THE SPECTRAL EVOLUTION ALONG THE Z TRACK OF THE BRIGHT NEUTRON STAR X-RAY BINARY GX 17+2

Dacheng Lin[1,2], Ronald A. Remillard[3], Jeroen Homan[3], and Didier Barret[1,2]
[1] CNRS, IRAP, 9 avenue du Colonel Roche, BP 44346, F-31028 Toulouse Cedex 4, France; Dacheng.Lin@irap.omp.eu
[2] Université de Toulouse, UPS-OMP, IRAP, F-31028 Toulouse Cedex 4, France
[3] MIT Kavli Institute for Astrophysics and Space Research, MIT, 70 Vassar Street, Cambridge, MA 02139-4307, USA
Received 2011 September 29; accepted 2012 June 29; published 2012 August 10

ABSTRACT

Z sources are bright neutron star X-ray binaries, accreting at around the Eddington limit. We analyze the 68 *RXTE* observations ($\sim$270 ks) of Sco-like Z source GX 17+2 made between 1999 October 3 and 12, covering a complete Z track. We create and fit color-resolved spectra with a model consisting of a thermal multicolor disk, a single-temperature-blackbody boundary layer and a weak Comptonized component. We find that, similar to what was observed for XTE J1701-462 in its Sco-like Z phase, the branches of GX 17+2 can be explained by three processes operating at a constant accretion rate $\dot{M}$ into the disk: increase of Comptonization up the horizontal branch (HB), transition from a standard thin disk to a slim disk up the normal branch (NB), and temporary fast decrease of the inner disk radius up the flaring branch. We also model the Comptonization in an empirically self-consistent way, with its seed photons tied to the thermal disk component and corrected for to recover the pre-Comptonized thermal disk emission. This allows us to show a constant $\dot{M}$ along the entire Z track based on the thermal disk component. We also measure the upper kHz quasi-periodic oscillation frequency and find it to depend on the apparent inner disk radius R_{in} (prior to Compton scattering) approximately as frequency $\propto R_{in}^{-3/2}$, supporting the identification of it as the Keplerian frequency at R_{in}. The HB oscillation is probably related to the dynamics in the inner disk as well, as both its frequency and R_{in} vary significantly on the HB but become relatively constant on the NB.

Key words: accretion, accretion disks – stars: individual (GX 17+2) – stars: neutron – X-rays: binaries – X-rays: bursts – X-rays: stars

Online-only material: color figures

1. INTRODUCTION

Based on the timing and spectral properties, six of the persistently bright neutron star (NS) low-mass X-ray binaries (LMXBs) were classified more than two decades ago as Z sources, named after the spectral evolution patterns they trace out in X-ray color–color diagrams (CDs) or hardness–intensity diagrams (HIDs; Hasinger & van der Klis 1989; van der Klis 2006). These sources are Sco X-1, GX 17+2, GX 349+2, GX 340+0, GX 5-1, and Cyg X-2. The upper, diagonal, and lower branches of their Z-shaped tracks are called horizontal, normal, and flaring branches (HB/NB/FB), respectively. Based on the shape and orientation of the Z tracks, these Z sources were further divided into two subgroups, with the first three called "Sco-like" Z sources and the latter three called "Cyg-like" (Kuulkers et al. 1994). The Sco-like Z sources have a more vertically oriented HB and a stronger FB than the Cyg-like types. The Z tracks themselves can also move and change shapes in the CDs/HIDs (secular changes), most substantially in the case of Cyg X-2.

Recently, XTE J1701-462 became the first X-ray transient identified as a Z source, and studies of this source have significantly improved our understanding of the spectral evolution in Z sources and their relation to atoll sources, another subclass of NS LMXBs with lower X-ray luminosity (L_X) than Z sources. XTE J1701-462 experienced a long outburst in 2006–2007, and it showed successive characteristics of Cyg-like Z, Sco-like Z, and atoll sources during the decay of the outburst (Homan et al. 2007, 2010; Lin et al. 2009, LRH09 hereafter). During these secular changes in the Z tracks, the upper (HB/NB) and lower (NB/FB) vertices each evolved along a specific line in the HID (LRH09). All three Z branches were present when the source was bright. During the decay, the HB, NB, and FB successively

disappeared, and the lower vertex finally transitioned into the atoll soft state.

Using an X-ray spectral model that was successfully applied to two atoll transients (Lin et al. 2007), LRH09 showed that it is most likely the mass accretion rate ($\dot{M}$) into the disk that drives the secular changes of Z tracks and the transitions from Z to atoll types. While the inner disk radius remained constant in the soft state of the atoll stage from the same spectral model, the inner disk radius in the Z stage increased with luminosity, which was interpreted as an effect of the local Eddington limit. On the other hand, the motion along a Z branch on short timescales appeared to operate at roughly constant $\dot{M}$, at least for Sco-like Z tracks (LRH09). Furthermore, the three Z branches were linked to different mechanisms by LRH09. The source ascends the HB as Comptonization of the disk emission increases. The apparent luminosity of the boundary layer increases along the NB from the lower to the upper vertices, which can be explained as a transition from a geometrically thin disk to a thick disk that is expected to admit an advective component of mass flow to the NS. The FB is traced out as the inner disk radius temporarily decreases toward the value seen in the atoll soft state, presumably the innermost stable circular orbit (ISCO).

In this work, we study GX 17+2. Figure 1 plots its long-term light curve from the *RXTE* All-Sky Monitor (ASM; Levine et al. 1996). The source shows a roughly constant level ($\sim$45 counts s^{-1}), with frequent flares on top, suggesting little change of the overall properties of this source over a long timescale. In fact, it shows very small secular changes (Wijnands et al. 1997; Homan et al. 2002), in contrast to XTE J1701-462.

X-ray spectral studies of GX 17+2 have been reported previously (Di Salvo et al. 2000; Farinelli et al. 2005; Migliari et al. 2007). Di Salvo et al. (2000) fitted the *BeppoSAX* spectra from the HB and NB with a single-temperature blackbody (BB)
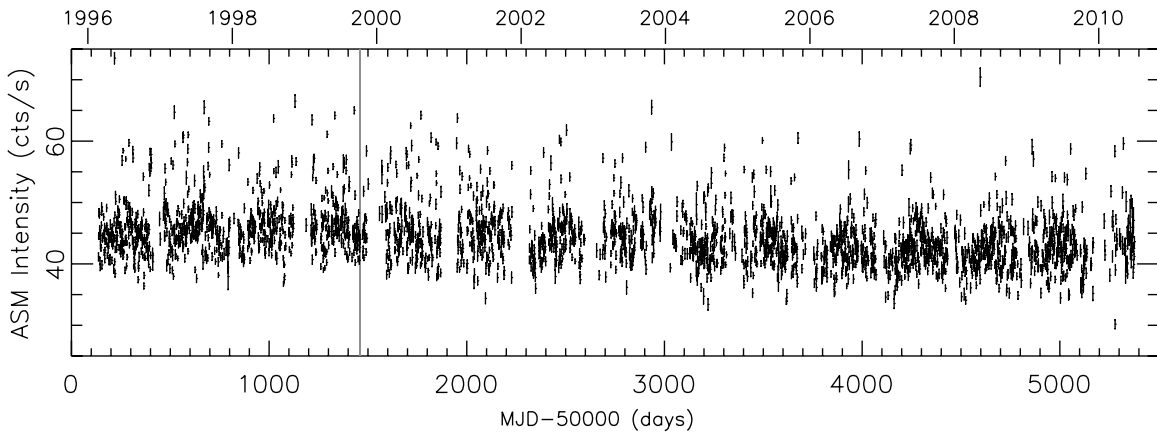
Figure 1. *RXTE* ASM one-day-averaged light curve of GX 17+2 spanning ∼14 years. The narrow gray region marks the interval UTC 1999-10-03.1–12.3, during which the PCA observations analyzed in the paper were obtained.

plus a Comptonized component for the continuum spectra. They found a hard tail on the HB, which was fit by a power law (PL) and contributed ∼8% of the 0.1–200 keV source flux. This component gradually faded as the source moved toward the NB, where it was no longer detectable (see also Farinelli et al. 2005). Migliari et al. (2007) carried out simultaneous radio and X-ray observations of GX 17+2 and found that a positive correlation between the radio flux density and the flux of the hard tail. Detailed timing analyses of GX 17+2 were made by Kuulkers et al. (1997), Wijnands et al. (1997), and Homan et al. (2002), with the evolution of various types of quasi-periodic oscillations (QPOs) along the Z track obtained.

Here, we carry out the spectral modeling of GX 17+2, in order to determine whether its spectral evolution is similar to that of the Sco-like Z stage in XTE J1701-462 (LRH09). As its secular changes are small, we just concentrate on a nine-day period of intensive *RXTE* pointed observations in 1999. Different from previous X-ray spectral modeling of this source, we use a low-Comptonization model dominated by a thermal disk and a thermal boundary layer component, because of its successes with atoll sources and XTE J1701-462 (Lin et al. 2007, 2010; LRH09). One main advantage of this model over other commonly used models (see Barret 2001 for a review) is that it infers the disk in the soft state of atoll sources to behave approximately as $L \propto T^4$, which is often seen in the thermal state of black hole X-ray binaries as well (Lin et al. 2007). We also compare our spectral fit results with the evolution of kHz QPOs and HB oscillations (HBOs) in order to obtain hints on the origins of these QPOs. GX 17+2 is more suitable than XTE J1701-462 for such a study, since such QPOs were not detected as frequently in the latter source (Homan et al. 2010; Sanna et al. 2010; Barret et al. 2011). In Section 2, we describe the reduction of the data and the procedure by which we create our spectra. The CDs and HIDs are also presented in this section. We describe the spectral models in Section 3. The spectral fit results and correlations with fast variability are given in Section 4. In Section 5, we discuss the mass accretion rate, the physical interpretation of spectral evolution, and the possible origins of kHz QPOs and HBOs. Finally, we present our conclusions.

2. DATA ANALYSES AND COLOR–COLOR DIAGRAMS

We analyzed 68 *RXTE* observations of GX 17+2 made between UTC 1999 October 3.1 and 12.3 (i.e., MJD 51454.1–51463.3), using the same standard criteria to filter

the data (e.g., removal of five type I X-ray bursts) as described in Lin et al. (2007). FTOOLS 6.9 was used. The source can move on timescales as short as minutes in the CD/HID, especially on the FB. To track the evolution along the Z track but also to gain enough statistics for spectral modeling and timing analysis, data are normally split into short exposures and then rebinned based on their positions in the CD/HID (e.g., LRH09; Homan et al. 2002). We also followed this procedure here. We calculated X-ray colors using the Proportional Counter Unit (PCU) 2 of the Proportional Counter Array (PCA; Jahoda et al. 1996), in the same way as described in Lin et al. (2007). The soft color (SC) and the hard color (HC) are defined as the ratios of the Crab-Nebula-normalized count rates in the (3.6–5.0)/(2.2–3.6) keV bands and the (8.6–18.0)/(5.0–8.6) keV bands, respectively. We used spectra with exposures of 32 s from the "standard 2" data to calculate the colors and construct the CD and HID, which are shown in the upper panels of Figure 2. The HB, NB, and FB are denoted by the blue square, green triangle, and red cross symbols, respectively, and this convention is used for all other figures in this paper.

Only a single Z track is seen in these diagrams. The lower parts of the NB and FB have substantial overlap. From the 2.2–3.6 keV and 8.6–18.0 keV light curves in Figure 3, we see that the source experienced frequent flares between MJD 51461.2 and 51463.3. We identified the data within this interval as the FB, as supported by their positions in the CD and HID in Figure 2. The transition from the HB to the NB is quite smooth. Their boundary is defined to be HC ≃ 0.45 (strictly $S_Z = 1$, see below). We note that the branches are hard to separate completely and that the above identification is approximate.

The data points are often assigned a rank number S_Z to track their positions along the Z track (Hasinger et al. 1990; Hertz et al. 1992). This can be done by creating splines along the Z track. Considering that the scattering is large in the CD (mostly due to large statistical uncertainties of SCs), we created the splines in the HID, which are shown in the top right panel of Figure 2. Due to large overlap of lower parts of the FB and the NB, we created a spline for the FB (the FB spline) and another one for the HB and NB (the HB+NB spline). We picked the normal points of the splines by hand, with one of them shared by the two splines. The S_Z value of this common normal point is set to be 2.0 (the lower vertex), while the point with HC = 0.45 in the HB+NB spline has $S_Z = 1.0$ (defined as the upper vertex and the boundary the HB and NB). S_Z values at other positions in the splines are determined based on their distances to these two points along
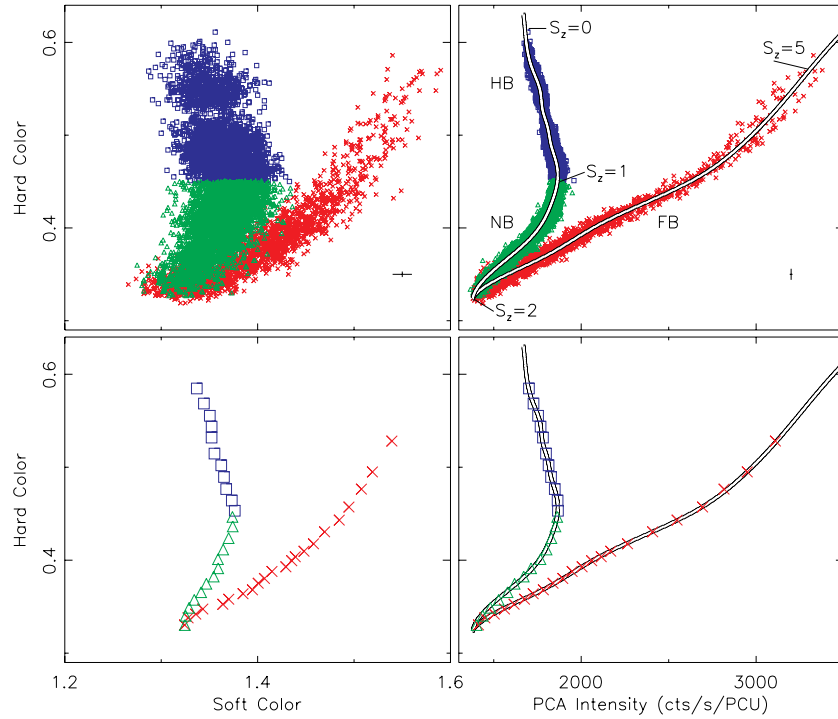
Figure 2. Color–color and hardness–intensity diagrams. The HB, NB, and FB are marked by blue squares, green triangles, and red crosses, respectively. Upper panels: 32 s spectra are used, and the splines that are used for the S_Z parameterization are shown in the HID. Lower panels: S_Z-resolved spectra are used, and the splines are repeated here for reference.

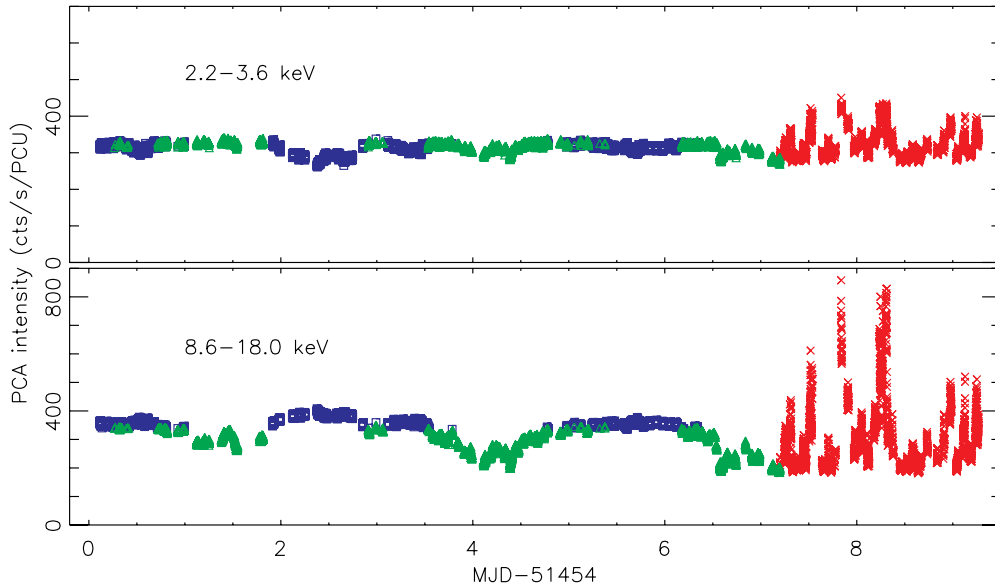(A color version of this figure is available in the online journal.)

Figure 3. *RXTE* PCA 32 s light curves in two energy bands. The typical error bars are smaller than the symbol size. The meanings of the symbols are the same as Figure 2.

(A color version of this figure is available in the online journal.)

the splines. Considering the different units of HC and intensity, we divide them by a characteristic number before calculating the distances, 0.45 for the HC and 2000 counts s^{-1} PCU^{-1} for the intensity. Finally, the values of S_Z for data points on the FB and on the HB and NB are obtained by projecting them onto the FB and the HB+NB splines, respectively. We note that in Homan et al. (2002) a single spline was used and was applied in the CD. This is due to the wider energy bands that they used to define the SCs. We chose to keep our definition of colors as

adopted in Lin et al. (2007) and LRH09 for easy comparison with these studies.

We then combined 32 s spectra from PCU 2 based on selections in S_Z to create spectra with longer exposures for our spectral fits. The ranges of S_Z and the exposures for these S_Z-resolved spectra are given in Tables 1 and 2. Their locations in the CD and HID are shown in the lower panels of Figure 2. We also created spectra of PCU 0 and those of the High Energy X-ray Timing Experiment (HEXTE; Rothschild et al. 1998),

Table 1
Spectral Fit Results Using Model 1

S_Z	EXP (ks)	kT_{MCD} (keV)	N_{MCD}	kT_{BB} (keV)	N_{BB}	N_{CPL}	σ_{line} (keV)	N_{line} (10^{-2})	EW (eV)	τ_{edge} (10^{-2})	$\chi^2_\nu(\nu)$	$L_{X,Edd}$
(1)	(2)	(3)	(4)	(5)	(6)	(7)	(8)	(9)	(10)	(11)	(12)	(13)
0.07–0.24	2.1	1.52 ± 0.05	85 ± 7	2.66 ± 0.04	14.7 ± 0.9	1.58 ± 0.11	0.36 ± 0.19	1.2 ± 0.3	77 ± 18	2.9 ± 1.4	0.75(151)	1.44 ± 0.06
0.24–0.32	2.3	1.56 ± 0.04	91 ± 7	2.69 ± 0.04	14.6 ± 0.9	1.30 ± 0.11	0.42 ± 0.20	$1.2^{+0.5}_{-0.3}$	76 ± 20	2.5 ± 1.5	0.78(149)	1.46 ± 0.05
0.32–0.40	5.7	1.58 ± 0.03	95 ± 6	2.66 ± 0.03	15.3 ± 0.8	1.23 ± 0.07	0.40 ± 0.19	1.1 ± 0.3	66 ± 17	3.1 ± 1.2	0.80(154)	1.48 ± 0.04
0.40–0.48	6.4	1.59 ± 0.03	97 ± 5	2.66 ± 0.03	15.3 ± 0.8	1.13 ± 0.07	0.36 ± 0.18	1.1 ± 0.3	63 ± 16	3.2 ± 1.2	0.86(155)	1.49 ± 0.04
0.48–0.56	3.1	1.63 ± 0.03	98 ± 6	2.70 ± 0.04	14.5 ± 0.8	0.92 ± 0.10	0.43 ± 0.21	$1.2^{+0.5}_{-0.3}$	72 ± 18	2.6 ± 1.5	0.96(146)	1.49 ± 0.05
0.56–0.64	3.0	1.64 ± 0.03	106 ± 5	2.68 ± 0.04	15.2 ± 0.9	0.71 ± 0.09	0.33 ± 0.21	1.0 ± 0.3	56 ± 14	2.5 ± 1.2	0.98(147)	1.51 ± 0.04
0.64–0.72	8.5	1.64 ± 0.02	108 ± 4	2.65 ± 0.03	15.4 ± 0.8	0.71 ± 0.06	0.36 ± 0.16	1.0 ± 0.2	60 ± 13	3.0 ± 1.1	1.01(147)	1.52 ± 0.03
0.72–0.80	16.7	1.64 ± 0.02	111 ± 4	2.60 ± 0.02	16.3 ± 0.8	0.74 ± 0.05	0.30 ± 0.18	1.0 ± 0.2	55 ± 14	3.8 ± 1.0	1.13(139)	1.53 ± 0.03
0.80–0.88	20.0	1.66 ± 0.02	113 ± 4	2.60 ± 0.02	16.3 ± 0.8	0.63 ± 0.05	0.31 ± 0.17	1.0 ± 0.2	57 ± 13	3.7 ± 1.0	1.06(142)	1.55 ± 0.03
0.88–0.96	24.8	1.67 ± 0.02	113 ± 4	2.59 ± 0.02	16.3 ± 0.8	0.56 ± 0.04	$0.27^{+0.15}_{-0.26}$	1.0 ± 0.2	54 ± 12	4.3 ± 1.0	1.03(140)	1.56 ± 0.02
0.96–1.00	9.1	1.71 ± 0.02	112 ± 4	2.62 ± 0.03	14.9 ± 0.9	0.40 ± 0.06	$0.30^{+0.15}_{-0.22}$	1.0 ± 0.2	54 ± 15	3.7 ± 1.0	0.88(146)	1.55 ± 0.03
1.00–1.04	8.0	1.70 ± 0.02	112 ± 4	2.60 ± 0.03	15.1 ± 1.0	0.42 ± 0.06	0.31 ± 0.18	1.0 ± 0.2	55 ± 14	3.8 ± 1.1	0.87(147)	1.55 ± 0.03
1.04–1.12	15.7	1.70 ± 0.02	117 ± 4	2.57 ± 0.03	15.5 ± 0.9	0.37 ± 0.04	$0.27^{+0.15}_{-0.26}$	0.9 ± 0.2	52 ± 13	4.2 ± 1.0	1.10(143)	1.54 ± 0.02
1.12–1.20	20.8	1.71 ± 0.02	117 ± 3	2.59 ± 0.03	14.2 ± 0.8	0.25 ± 0.04	$0.25^{+0.15}_{-0.25}$	0.9 ± 0.2	53 ± 12	4.0 ± 1.0	1.04(141)	1.53 ± 0.02
1.20–1.28	16.0	1.71 ± 0.02	118 ± 4	2.57 ± 0.03	13.6 ± 0.9	0.25 ± 0.04	$0.27^{+0.15}_{-0.26}$	0.9 ± 0.2	52 ± 12	4.4 ± 1.0	0.98(144)	1.51 ± 0.02
1.28–1.36	6.9	1.71 ± 0.02	118 ± 4	2.58 ± 0.04	12.8 ± 1.0	0.20 ± 0.06	$0.29^{+0.15}_{-0.24}$	0.9 ± 0.2	52 ± 13	4.5 ± 1.1	0.94(134)	1.48 ± 0.03
1.36–1.44	6.5	1.70 ± 0.02	118 ± 4	2.52 ± 0.04	12.9 ± 1.2	0.26 ± 0.06	$0.28^{+0.14}_{-0.21}$	0.9 ± 0.2	57 ± 14	5.7 ± 1.1	0.99(136)	1.44 ± 0.03
1.44–1.52	6.1	1.68 ± 0.02	120 ± 4	2.49 ± 0.05	12.6 ± 1.3	0.29 ± 0.05	0.28 ± 0.16	1.0 ± 0.2	62 ± 14	5.5 ± 1.1	1.12(141)	1.41 ± 0.03
1.52–1.60	5.2	1.69 ± 0.02	118 ± 4	2.55 ± 0.05	10.7 ± 1.1	0.20 ± 0.06	0.30 ± 0.14	1.1 ± 0.2	70 ± 14	5.1 ± 1.2	1.02(134)	1.37 ± 0.03
1.60–1.68	5.8	1.70 ± 0.02	115 ± 4	2.57 ± 0.05	9.3 ± 1.0	0.20 ± 0.06	0.31 ± 0.14	1.1 ± 0.2	73 ± 14	5.0 ± 1.2	1.22(131)	1.34 ± 0.03
1.68–1.76	3.0	1.67 ± 0.02	121 ± 4	2.54 ± 0.06	9.7 ± 1.2	0.15 ± 0.07	0.34 ± 0.11	1.3 ± 0.2	86 ± 16	5.4 ± 1.3	1.26(126)	1.31 ± 0.03
1.76–1.84	3.1	1.68 ± 0.02	116 ± 4	2.56 ± 0.07	8.4 ± 1.1	0.15 ± 0.07	0.35 ± 0.11	1.3 ± 0.2	95 ± 16	5.7 ± 1.3	0.99(130)	1.27 ± 0.03
1.84–1.92	2.6	1.70 ± 0.02	112 ± 4	2.64 ± 0.07	$6.9^{+1.0}_{-0.5}$	$0.05^{+0.08}_{-0.05}$	0.35 ± 0.10	1.4 ± 0.2	105 ± 17	5.6 ± 1.4	0.98(120)	1.23 ± 0.03
1.92–2.00	0.7	$1.72^{+0.02}_{-0.04}$	107^{+8}_{-5}	$2.67^{+0.08}_{-0.14}$	$5.8^{+1.6}_{-0.9}$	$0.06^{+0.14}_{-0.06}$	0.35 ± 0.13	1.5 ± 0.3	113 ± 22	6.3 ± 2.1	0.90(111)	1.21 ± 0.05
2.00–2.08	2.3	1.70 ± 0.02	112 ± 4	2.61 ± 0.07	6.9 ± 0.9	$0.04^{+0.08}_{-0.04}$	0.35 ± 0.09	1.6 ± 0.2	118 ± 17	6.1 ± 1.5	1.02(122)	1.21 ± 0.03
2.08–2.16	7.6	1.71 ± 0.02	111 ± 3	$2.62^{+0.03}_{-0.05}$	7.1 ± 0.7	0.04 ± 0.04	0.34 ± 0.08	1.6 ± 0.2	118 ± 14	5.8 ± 1.2	1.39(128)	1.23 ± 0.02
2.16–2.24	6.5	1.73 ± 0.02	107 ± 3	2.55 ± 0.06	8.2 ± 1.0	0.13 ± 0.05	0.33 ± 0.08	1.7 ± 0.2	117 ± 14	7.1 ± 1.2	1.17(131)	1.27 ± 0.03
2.24–2.32	5.4	1.75 ± 0.02	103 ± 4	2.58 ± 0.06	8.3 ± 1.0	0.08 ± 0.06	0.40 ± 0.08	1.9 ± 0.2	128 ± 17	6.2 ± 1.3	1.27(127)	1.30 ± 0.03
2.32–2.40	3.8	1.82 ± 0.02	93 ± 3	2.64 ± 0.08	7.4 ± 1.1	0.08 ± 0.08	0.34 ± 0.08	1.9 ± 0.2	123 ± 14	7.0 ± 1.2	1.15(125)	1.34 ± 0.04
2.40–2.48	3.0	1.84 ± 0.03	93 ± 3	$2.66^{+0.04}_{-0.08}$	$7.7^{+1.3}_{-0.6}$	$0.02^{+0.09}_{-0.02}$	0.39 ± 0.08	2.1 ± 0.3	128 ± 18	6.2 ± 1.3	1.33(123)	1.38 ± 0.03
2.48–2.56	3.2	1.88 ± 0.03	87 ± 3	2.67 ± 0.08	7.5 ± 1.2	0.08 ± 0.08	0.35 ± 0.08	2.0 ± 0.2	119 ± 16	7.0 ± 1.2	1.44(130)	1.41 ± 0.04
2.56–2.64	1.9	1.92 ± 0.03	83^{+3}_{-1}	$2.76^{+0.05}_{-0.08}$	$6.7^{+1.2}_{-0.8}$	$0.00^{+0.10}$	0.36 ± 0.08	2.1 ± 0.2	118 ± 16	7.6 ± 1.3	1.31(129)	1.44 ± 0.03
2.64–2.72	2.6	1.96 ± 0.03	78 ± 3	$2.75^{+0.05}_{-0.10}$	$6.6^{+1.4}_{-0.9}$	$0.05^{+0.11}_{-0.05}$	0.35 ± 0.09	2.0 ± 0.3	111 ± 13	7.0 ± 1.3	1.44(128)	1.48 ± 0.04
2.72–2.80	3.1	1.99 ± 0.02	76 ± 3	$2.80^{+0.04}_{-0.07}$	6.4 ± 0.8	$0.00^{+0.07}$	0.34 ± 0.09	2.1 ± 0.3	112 ± 14	6.8 ± 1.1	1.41(128)	1.51 ± 0.03
2.80–2.88	2.5	2.00 ± 0.03	75 ± 3	2.77 ± 0.05	7.2 ± 1.0	$0.00^{+0.06}$	$0.36^{+0.08}_{-0.05}$	2.2 ± 0.3	110 ± 16	6.7 ± 1.2	1.41(128)	1.55 ± 0.03
2.88–2.96	2.3	2.04 ± 0.03	71^{+3}_{-1}	$2.81^{+0.05}_{-0.09}$	$6.7^{+1.4}_{-0.9}$	$0.00^{+0.10}$	0.36 ± 0.09	2.2 ± 0.3	111 ± 15	6.8 ± 1.3	1.25(130)	1.58 ± 0.04
2.96–3.04	1.9	2.06 ± 0.03	69 ± 3	2.81 ± 0.05	7.0 ± 1.1	$0.00^{+0.04}$	0.32 ± 0.10	2.2 ± 0.3	105 ± 15	7.2 ± 1.2	1.42(122)	1.62 ± 0.03
3.04–3.12	1.9	2.10 ± 0.04	66^{+3}_{-2}	2.82 ± 0.07	6.8 ± 1.3	$0.00^{+0.10}$	0.38 ± 0.10	2.2 ± 0.3	104 ± 17	7.1 ± 1.2	1.33(123)	1.65 ± 0.04
3.12–3.20	1.4	2.16 ± 0.04	62 ± 3	$2.89^{+0.08}_{-0.04}$	$5.8^{+0.6}_{-1.1}$	$0.00^{+0.05}$	0.35 ± 0.09	2.2 ± 0.3	97 ± 15	7.3 ± 1.3	1.25(125)	1.69 ± 0.03
3.20–3.40	2.5	2.17 ± 0.04	62 ± 3	2.86 ± 0.06	6.8 ± 1.2	$0.00^{+0.05}$	0.38 ± 0.10	2.3 ± 0.4	100 ± 18	7.0 ± 1.3	1.39(126)	1.77 ± 0.04
3.40–3.60	2.0	2.27 ± 0.05	55^{+4}_{-2}	2.98 ± 0.08	5.3 ± 1.3	$0.00^{+0.07}$	0.38 ± 0.10	2.3 ± 0.4	94 ± 15	6.4 ± 1.2	1.26(131)	1.85 ± 0.05
3.60–3.80	1.3	2.36 ± 0.06	51 ± 3	3.04 ± 0.12	4.4 ± 1.5	$0.00^{+0.06}$	0.39 ± 0.10	2.2 ± 0.4	84 ± 18	6.3 ± 1.3	1.33(118)	1.95 ± 0.06
3.80–4.00	1.1	2.44 ± 0.07	47^{+4}_{-2}	3.09 ± 0.17	$4.2^{+2.0}_{-1.1}$	$0.00^{+0.10}$	0.39 ± 0.10	2.4 ± 0.4	87 ± 17	6.5 ± 1.2	1.25(128)	2.06 ± 0.08
4.00–4.20	0.9	2.55 ± 0.08	42 ± 3	3.22 ± 0.21	$3.2^{+1.9}_{-1.1}$	$0.00^{+0.07}$	0.41 ± 0.11	2.4 ± 0.5	83 ± 18	5.2 ± 1.3	1.38(121)	2.14 ± 0.08
4.20–4.40	1.0	$2.68^{+0.06}_{-0.13}$	37^{+5}_{-2}	3.34 ± 0.27	$2.3^{+3.0}_{-1.2}$	$0.00^{+0.08}$	0.44 ± 0.11	2.5 ± 0.5	82 ± 21	5.3 ± 1.1	1.12(125)	2.23 ± 0.11
4.40–4.80	1.1	$2.90^{+0.06}_{-0.17}$	29^{+5}_{-1}	$3.53^{+0.78}_{-0.25}$	$1.0^{+3.3}_{-0.9}$	$0.00^{+0.06}$	0.44 ± 0.12	2.5 ± 0.3	77 ± 19	4.2 ± 1.1	1.02(127)	2.34 ± 0.14

Notes. The first column is the S_Z range of each spectrum. The second column is the exposure per PCU. The last column is the total luminosity in units of the Eddington luminosity (3.79×10^{38} erg s^{-1}; Section 4.3). See the text for the meanings of other columns.

which match the spectra of PCU 2 in time. PCUs 0 and 2 were the only units that were operating during all of our observations. For the HEXTE, we used both Clusters A and B. We applied dead time corrections to both the PCA and HEXTE data.

We also created power density spectra (PDSs), which match the S_Z-resolved spectra in time, to search for the kHz QPOs and HBOs and study their relations with our spectral fit parameters. As we used a different way of data reduction from Homan

Table 2
Spectral Fit Results Using Model 2

S_Z	kT_{MCD} (keV)	N_{MCD}	N_{MCDPS}	kT_{BB} (keV)	N_{BB}	$N_{nthComp}$	σ_{line} (keV)	N_{line} (10^{-2})	EW (eV)	τ_{edge} (10^{-2})	$\chi^2_\nu(\nu)$	$L_{X,Edd}$
(1)	(2)	(3)	(4)	(5)	(6)	(7)	(8)	(9)	(10)	(11)	(12)	(13)
0.07–0.24	1.32 ± 0.04	124 ± 9	232 ± 27	2.59 ± 0.04	$16.3^{+0.9}_{-1.4}$	0.94 ± 0.09	$0.43^{+0.28}_{-0.17}$	$1.4^{+1.1}_{-0.3}$	89 ± 19	3.3 ± 1.5	0.83(151)	1.48 ± 0.06
0.24–0.32	1.42 ± 0.04	132^{+10}_{-15}	195 ± 19	$2.65^{+0.03}_{-0.06}$	$15.4^{+1.4}_{-0.5}$	0.67 ± 0.07	$0.81^{+0.14}_{-0.46}$	$2.4^{+0.5}_{-1.2}$	148 ± 43	$0.1^{+3.6}_{-0.1}$	0.86(149)	1.47 ± 0.05
0.32–0.40	1.45 ± 0.03	124^{+11}_{-7}	178 ± 14	$2.61^{+0.02}_{-0.03}$	16.7 ± 0.8	0.62 ± 0.05	$0.49^{+0.38}_{-0.19}$	$1.3^{+1.1}_{-0.3}$	78 ± 20	$2.9^{+1.4}_{-2.9}$	0.86(154)	1.50 ± 0.04
0.40–0.48	1.49 ± 0.03	122 ± 6	167 ± 12	2.61 ± 0.03	16.7 ± 0.8	0.55 ± 0.04	0.42 ± 0.20	$1.2^{+0.5}_{-0.3}$	71 ± 18	3.1 ± 1.4	0.90(155)	1.51 ± 0.04
0.48–0.56	$1.50^{+0.07}_{-0.03}$	131^{+7}_{-17}	165^{+12}_{-23}	2.67 ± 0.04	$15.5^{+1.1}_{-0.7}$	0.42 ± 0.05	$0.81^{+0.14}_{-0.46}$	$2.3^{+0.5}_{-1.2}$	138 ± 43	$0.1^{+3.3}_{-0.1}$	1.01(146)	1.51 ± 0.05
0.56–0.64	1.58 ± 0.03	122 ± 6	144 ± 10	2.63 ± 0.04	16.3 ± 1.0	0.32 ± 0.05	0.36 ± 0.20	1.0 ± 0.3	60 ± 15	2.4 ± 1.3	0.99(147)	1.52 ± 0.05
0.64–0.72	1.58 ± 0.03	124 ± 5	145 ± 8	2.61 ± 0.03	16.5 ± 0.8	0.31 ± 0.03	0.39 ± 0.16	1.1 ± 0.3	63 ± 16	2.8 ± 1.1	0.97(147)	1.53 ± 0.03
0.72–0.80	1.58 ± 0.02	127 ± 5	149 ± 7	2.57 ± 0.02	17.5 ± 0.8	0.32 ± 0.02	0.32 ± 0.17	1.0 ± 0.2	57 ± 14	3.7 ± 1.0	1.06(139)	1.54 ± 0.02
0.80–0.88	1.61 ± 0.02	126 ± 5	144 ± 6	2.57 ± 0.02	17.3 ± 0.8	0.26 ± 0.02	0.33 ± 0.17	1.1 ± 0.2	59 ± 14	3.5 ± 1.0	1.01(142)	1.55 ± 0.02
0.88–0.96	1.63 ± 0.02	125 ± 4	139 ± 6	2.56 ± 0.02	17.3 ± 0.9	0.23 ± 0.02	$0.29^{+0.15}_{-0.24}$	1.0 ± 0.2	55 ± 12	4.1 ± 1.0	0.98(140)	1.56 ± 0.02
0.96–1.00	1.67 ± 0.02	120 ± 5	129 ± 6	2.60 ± 0.03	15.7 ± 1.0	0.16 ± 0.02	0.31 ± 0.18	1.0 ± 0.2	56 ± 14	3.6 ± 1.0	0.84(146)	1.56 ± 0.03
1.00–1.04	1.67 ± 0.02	122 ± 5	132 ± 6	2.57 ± 0.03	16.1 ± 1.1	0.17 ± 0.02	0.33 ± 0.18	1.0 ± 0.2	56 ± 14	3.7 ± 1.1	0.83(147)	1.55 ± 0.02
1.04–1.12	1.67 ± 0.02	125 ± 4	134 ± 5	2.54 ± 0.03	16.4 ± 1.0	0.15 ± 0.02	$0.28^{+0.15}_{-0.28}$	1.0 ± 0.2	53 ± 12	4.1 ± 1.0	1.03(143)	1.55 ± 0.02
1.12–1.20	1.69 ± 0.02	123 ± 4	129 ± 5	2.57 ± 0.03	14.9 ± 0.9	0.10 ± 0.02	$0.26^{+0.15}_{-0.26}$	1.0 ± 0.2	53 ± 12	4.0 ± 1.0	0.98(141)	1.53 ± 0.02
1.20–1.28	1.69 ± 0.02	123 ± 4	129 ± 5	2.55 ± 0.03	14.3 ± 1.0	0.10 ± 0.02	$0.28^{+0.15}_{-0.28}$	0.9 ± 0.2	52 ± 12	4.3 ± 1.0	0.93(144)	1.51 ± 0.02
1.28–1.36	1.69 ± 0.02	123 ± 5	127 ± 6	2.55 ± 0.04	13.5 ± 1.2	0.08 ± 0.02	$0.30^{+0.15}_{-0.23}$	0.9 ± 0.2	53 ± 13	4.5 ± 1.1	0.90(134)	1.48 ± 0.03
1.36–1.44	1.67 ± 0.03	125 ± 5	131 ± 6	2.49 ± 0.05	13.7 ± 1.4	0.11 ± 0.02	$0.28^{+0.14}_{-0.21}$	1.0 ± 0.2	57 ± 13	5.7 ± 1.1	0.94(136)	1.44 ± 0.03
1.44–1.52	1.66 ± 0.03	127 ± 5	134 ± 6	2.46 ± 0.05	13.6 ± 1.4	0.12 ± 0.02	$0.29^{+0.13}_{-0.19}$	1.0 ± 0.2	63 ± 13	5.5 ± 1.1	1.06(141)	1.42 ± 0.03
1.52–1.60	1.67 ± 0.02	123 ± 5	128 ± 6	2.52 ± 0.05	11.4 ± 1.3	0.08 ± 0.02	0.31 ± 0.14	1.1 ± 0.2	70 ± 14	5.1 ± 1.2	0.99(134)	1.37 ± 0.03
1.60–1.68	1.68 ± 0.02	120 ± 4	124 ± 6	2.54 ± 0.06	9.9 ± 1.1	0.08 ± 0.02	0.31 ± 0.14	1.1 ± 0.2	74 ± 15	4.9 ± 1.2	1.18(131)	1.34 ± 0.03
1.68–1.76	1.65 ± 0.03	125 ± 5	130 ± 7	2.50 ± 0.07	10.3 ± 1.4	0.07 ± 0.03	0.34 ± 0.11	1.3 ± 0.2	87 ± 14	5.4 ± 1.3	1.23(126)	1.31 ± 0.03
1.76–1.84	1.67 ± 0.03	120 ± 5	124 ± 6	2.52 ± 0.07	9.0 ± 1.3	0.07 ± 0.03	0.35 ± 0.11	1.4 ± 0.2	96 ± 16	5.7 ± 1.3	0.96(130)	1.27 ± 0.03
1.84–1.92	1.69 ± 0.03	114 ± 4	115 ± 6	2.60 ± 0.08	7.3 ± 1.1	0.03 ± 0.03	0.36 ± 0.10	1.4 ± 0.2	106 ± 17	5.7 ± 1.4	0.97(120)	1.23 ± 0.04
1.92–2.00	1.70 ± 0.04	109 ± 6	112 ± 9	2.61 ± 0.14	$6.4^{+2.1}_{-1.4}$	0.04 ± 0.05	0.35 ± 0.12	1.5 ± 0.3	113 ± 23	6.5 ± 2.1	0.88(111)	1.20 ± 0.06
2.00–2.08	1.69 ± 0.03	114 ± 5	115 ± 6	2.58 ± 0.08	7.3 ± 1.2	0.03 ± 0.03	0.35 ± 0.09	1.6 ± 0.2	118 ± 17	6.2 ± 1.4	1.01(122)	1.21 ± 0.03
2.08–2.16	1.70 ± 0.02	112 ± 4	113 ± 4	2.61 ± 0.06	7.3 ± 0.8	0.02 ± 0.02	0.34 ± 0.08	1.6 ± 0.2	118 ± 15	5.9 ± 1.2	1.38(128)	1.23 ± 0.02
2.16–2.24	1.71 ± 0.02	110 ± 4	113 ± 5	2.52 ± 0.06	8.7 ± 1.2	0.05 ± 0.02	0.33 ± 0.08	1.7 ± 0.2	118 ± 14	7.1 ± 1.2	1.15(131)	1.27 ± 0.03
2.24–2.32	1.74 ± 0.03	106 ± 4	108 ± 5	2.56 ± 0.07	8.7 ± 1.2	0.03 ± 0.02	0.40 ± 0.08	1.9 ± 0.2	129 ± 17	6.2 ± 1.2	1.25(127)	1.31 ± 0.03
2.32–2.40	1.80 ± 0.03	96 ± 4	98 ± 5	2.59 ± 0.08	8.1 ± 1.4	0.04 ± 0.02	0.34 ± 0.08	2.0 ± 0.2	124 ± 16	7.1 ± 1.2	1.12(125)	1.34 ± 0.04
2.40–2.48	1.82 ± 0.03	95 ± 4	95 ± 5	$2.62^{+0.05}_{-0.08}$	8.3 ± 1.4	0.02 ± 0.02	0.39 ± 0.08	2.1 ± 0.3	129 ± 16	6.3 ± 1.3	1.33(123)	1.38 ± 0.04
2.48–2.56	1.85 ± 0.03	89 ± 4	91 ± 5	2.61 ± 0.09	8.4 ± 1.6	0.04 ± 0.03	0.35 ± 0.08	2.0 ± 0.2	120 ± 15	7.1 ± 1.2	1.41(130)	1.41 ± 0.04
2.56–2.64	1.90 ± 0.04	84 ± 4	85 ± 5	2.69 ± 0.10	7.4 ± 1.5	$0.02^{+0.03}$	0.36 ± 0.09	2.1 ± 0.3	118 ± 16	7.8 ± 1.3	1.30(129)	1.44 ± 0.05
2.64–2.72	1.93 ± 0.04	81 ± 4	82 ± 5	2.67 ± 0.11	7.7 ± 1.7	0.04 ± 0.03	0.35 ± 0.09	2.1 ± 0.3	112 ± 15	7.1 ± 1.2	1.42(128)	1.48 ± 0.05
2.72–2.80	1.98 ± 0.03	77 ± 3	77 ± 4	$2.77^{+0.06}_{-0.11}$	6.7 ± 1.4	$0.01^{+0.03}$	0.34 ± 0.09	2.1 ± 0.3	112 ± 16	6.8 ± 1.2	1.41(128)	1.52 ± 0.04
2.80–2.88	2.00 ± 0.04	75 ± 3	75^{+5}_{-3}	2.76 ± 0.10	$7.3^{+1.9}_{-1.0}$	$0.00^{+0.03}$	0.36 ± 0.09	2.2 ± 0.3	111 ± 16	6.7 ± 1.2	1.41(128)	1.55 ± 0.04
2.88–2.96	2.02 ± 0.05	73 ± 4	74 ± 5	2.73 ± 0.12	7.8 ± 1.9	$0.03^{+0.03}$	0.36 ± 0.09	2.3 ± 0.3	112 ± 16	6.9 ± 1.2	1.23(130)	1.59 ± 0.05
2.96–3.04	$2.06^{+0.03}_{-0.02}$	70 ± 3	70^{+1}_{-2}	2.79 ± 0.06	7.3 ± 1.2	$0.00^{+0.02}$	$0.33^{+0.08}_{-0.12}$	2.2 ± 0.3	105 ± 14	7.3 ± 1.3	1.42(122)	1.63 ± 0.03
3.04–3.12	2.08 ± 0.06	68 ± 4	69 ± 5	2.74 ± 0.12	7.9 ± 2.3	$0.02^{+0.03}$	0.38 ± 0.10	2.3 ± 0.3	105 ± 19	7.2 ± 1.3	1.33(123)	1.66 ± 0.06
3.12–3.20	2.15 ± 0.04	62 ± 3	62 ± 3	$2.88^{+0.08}_{-0.12}$	$6.0^{+1.7}_{-1.2}$	$0.00^{+0.03}$	0.35 ± 0.10	2.2 ± 0.3	97 ± 16	7.3 ± 1.3	1.25(125)	1.68 ± 0.05
3.20–3.40	2.17 ± 0.05	62 ± 3	62 ± 4	$2.85^{+0.06}_{-0.12}$	$7.0^{+2.2}_{-1.2}$	$0.00^{+0.03}$	0.38 ± 0.09	2.3 ± 0.3	100 ± 17	7.0 ± 1.2	1.39(126)	1.75 ± 0.05
3.40–3.60	2.26 ± 0.06	57 ± 4	57 ± 4	$2.92^{+0.11}_{-0.17}$	$5.9^{+2.8}_{-1.6}$	$0.01^{+0.04}$	0.38 ± 0.11	2.3 ± 0.4	94 ± 16	6.5 ± 1.2	1.25(131)	1.86 ± 0.08
3.60–3.80	$2.36^{+0.05}_{-0.09}$	51 ± 3	51^{+6}_{-3}	$3.03^{+0.13}_{-0.24}$	$4.6^{+3.6}_{-1.5}$	$0.00^{+0.05}$	0.40 ± 0.12	2.2 ± 0.4	84 ± 19	6.3 ± 1.2	1.33(118)	1.97 ± 0.10
3.80–4.00	2.39 ± 0.12	49^{+8}_{-5}	50^{+9}_{-5}	2.91 ± 0.27	$6.0^{+6.3}_{-3.2}$	$0.04^{+0.04}$	0.40 ± 0.13	2.5 ± 0.5	88 ± 19	6.6 ± 1.3	1.24(128)	2.06 ± 0.16
4.00–4.20	$2.54^{+0.08}_{-0.16}$	42^{+7}_{-3}	43^{+8}_{-3}	3.16 ± 0.35	$3.5^{+5.8}_{-0.5}$	$0.01^{+0.07}$	0.41 ± 0.13	2.4 ± 0.4	83 ± 20	5.3 ± 1.3	1.38(121)	2.14 ± 0.15
4.20–4.40	$2.62^{+0.11}_{-0.22}$	38^{+9}_{-3}	39^{+10}_{-4}	$3.14^{+0.60}_{-0.38}$	$3.6^{+8.2}_{-2.4}$	$0.02^{+0.06}$	0.44 ± 0.14	2.6 ± 0.5	83 ± 20	5.4 ± 1.3	1.12(125)	2.23 ± 0.21
4.40–4.80	$2.89^{+0.05}_{-0.31}$	29^{+5}_{-1}	29^{+10}_{-1}	3.49 ± 0.71	$1.1^{+9.3}_{-0.2}$	$0.00^{+0.05}$	0.44 ± 0.13	2.5 ± 0.5	77 ± 21	4.2 ± 1.2	1.02(127)	2.33 ± 0.24

Note. See the text and Table 1 for the meaning of each column.

et al. (2002), our PDS do not match theirs in time. We used the PCA event files to create 5.8–40 keV light curves (from all available PCUs) in a time bin of 2^{-12} s. We then calculated S_Z-resolved PDS by averaging the individual PDS computed for

the appropriate set of 32 s time intervals. We excluded events below 5.8 keV to increase the detection significance of QPOs, as in Homan et al. (2002). We refer to their paper for more information on the data modes of the event files. We then fitted

the PDS in a very similar way as Homan et al. (2002) to search for kHz QPOs and HBOs. Basically, the 200–2048 Hz PDSs were fitted with one or two Lorentzians for the kHz QPOs plus a dead-time-modified Poisson level, and the 0.03125–256 Hz PDSs were fitted with a PL, a cutoff PL (CPL), and/or a Lorentzian for various broad noise components and Lorentzians for QPOs, including HBOs, plus a constant for the Poisson level. We also calculated the rms within the 0.1–10 Hz frequency band from these PDS, in order to study its correlation with the Comptonization fraction inferred from the spectral parameters.

As the PCA does not cover the low energy band below 2.5 keV and has only a modest energy resolution, we also analyzed two *Suzaku* observations (sequence numbers 402050010 and 402050020), using the same data reduction procedure as in Lin et al. (2010), to help to estimate the absorption and the Fe line energy for our spectral fits to the *RXTE* data. The calibration files of 2010 June and *Suzaku* FTOOLS version 15 were used. Spectra from XIS (Koyama et al. 2007) 0 and 3 were extracted, with the central region of a radius of 55 pixels excluded to reduce the event pileup effect. XIS 1 was not used as it was in the full window mode, resulting in serious event pileup. We also used the spectra of the PIN diodes of the Hard X-ray Detector (Takahashi et al. 2007).

3. SPECTRAL MODELING

The S_Z-resolved PCA (PCU 0 and PCU 2) and HEXTE (Clusters A and B) spectra were fitted jointly, with their relative normalizations allowed to float. We used the energy range 2.9–40.0 keV for the PCA spectra and 20.0–60.0 keV for the HEXTE spectra. We assumed a model systematic error of 0.5%, as recommended by the PCA team. Both PCA and HEXTE data were binned to have at least 40 counts per bin. All error bars of spectral fit results quoted are at a 90% confidence level, unless indicated otherwise.

We fitted the spectra with a model consisting of a BB (*bbodyrad* in XSPEC), used to describe the boundary layer, a multicolor disk (MCD) BB (*diskbb* in XSPEC), and a weak Comptonized component. It also includes an Fe K Gaussian line, an Fe K absorption edge, and an interstellar medium absorption, described by the *gaussian*, *edge*, and *wabs* models in XSPEC, respectively. The absorption edge was included in Di Salvo et al. (2000) in their fits to the *BeppoSAX* spectra, and we found that including it in our model also improved our fits significantly (χ^2 decreases by about 37 on average for each S_Z-resolved spectrum, with 130 degrees of freedom (dof) typically). To reduce the scattering of our results, we used fixed values of the hydrogen column density $N_H = 2.35 \times 10^{22}$ cm^{-2}, the Gaussian line central energy $E_{ga} = 6.64$ keV, and the edge energy $E_{edge} = 8.93$ keV (derived below and at the end of this section) for all fits. We explored several descriptions of the Comptonized component. It is significant on the HB, and understanding this component is important toward our understanding of the HB, the HBOs, and the kHz QPOs.

The use of three spectral components to fit X-ray spectra of accreting NSs in the soft state must be done carefully (see Lin et al. 2007). The Comptonized and the thermal components can become degenerate when the Comptonized component is steep (e.g., the photon index larger than 2.5 when the Comptonization is modeled as a PL). Here, we first used a CPL (*cutoffpl* in XSPEC) to describe the Comptonized component. The whole model is *wabs(diskbb + bbodyrad + cutoffpl + gaussian)edge* using the XSPEC terminology, and this is our first model (Model 1, or model MCD+BB+CPL, hereafter). Using this
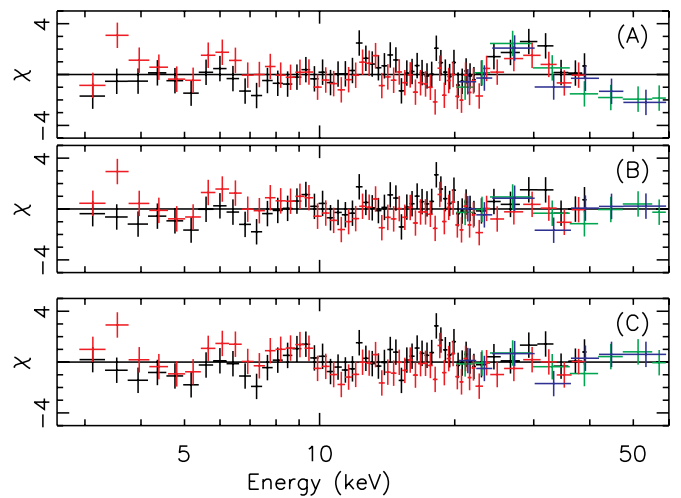

Figure 4. Fit residuals in terms of sigma for the spectrum with $S_Z = 0.32$–0.40, using various models for the Comptonization (see the text for details). This spectrum is used considering its large Comptonization fraction and exposure. (A) a PL, $\chi^2_\nu = 1.13$; (B) a CPL, i.e., Model 1, $\chi^2_\nu = 0.80$; and (C) an nthComp, i.e., Model 2, $\chi^2_\nu = 0.86$. The black, red, green, and blue data points are for the PCU 2, PCU 0, HEXTE Clusters A and B, respectively.

(A color version of this figure is available in the online journal.)

model, the Comptonized component turned out to be weak compared with the thermal components except at the top of the HB. The photon index Γ_{CPL} and the *e*-folding energy E_{CPL} were generally not well constrained from the fits, and they showed no clear sign of variation along the Z track. To have a better constrained estimate of them, we fitted all the HB spectra simultaneously with these two parameters tied to be the same and obtained $\Gamma_{CPL} = 1.40 \pm 0.14$ and $E_{CPL} = 9.9 \pm 1.0$ keV. These values were fixed in the final fits to all spectra. We then obtained $E_{edge} = 8.93 \pm 0.03$ keV from the simultaneous fit to the spectra from all branches. Although fits with the Comptonized component described by a PL can also have the χ^2_ν values around one, such fits have systematic residuals above 20 keV on the HB (Figure 4), which are significantly reduced using a CPL. The χ^2 decrease is 51.7, from 173.5 (dof = 153) to 121.8, for the $S_Z = 0.32$–0.40 spectrum. Applying the posterior predictive *p*-value method (Hurkett et al. 2008; Protassov et al. 2002) to this spectrum, we found that the reduction of χ^2 from the introduction of E_{CPL} is less than 15 for all 10^4 spectra that we simulated. Thus, the exponential rollover is required for the Comptonized component at a confidence level above 99.99% (at least for the $S_Z = 0.32$–0.40 spectrum). Figure 5(a) shows the unfolded spectra and fit residuals at four representative positions of the Z track (the top of the HB, the upper vertex, the lower vertex, and the top of the FB) using Model 1.

Next, we attempted to describe the Comptonization in a self-consistent way. Considering that the CPL luminosity variation along the HB is strongly anti-correlated with the disk luminosity from Model 1 (Section 4), we assumed the scenario that there is a corona above the disk so that some photons from the thermal disk emission are scattered by the hot electrons in it and turned into Comptonization emission. Such a picture has been suggested in some studies of black hole X-ray binaries and can be modeled with the SIMPL model (in XSPEC; Steiner et al. 2009a, 2009b). SIMPL is an empirical convolution model of Comptonization in which a fraction of the photons from an input seed spectrum are scattered into a PL component with the rest are unscattered and observed directly. While applying
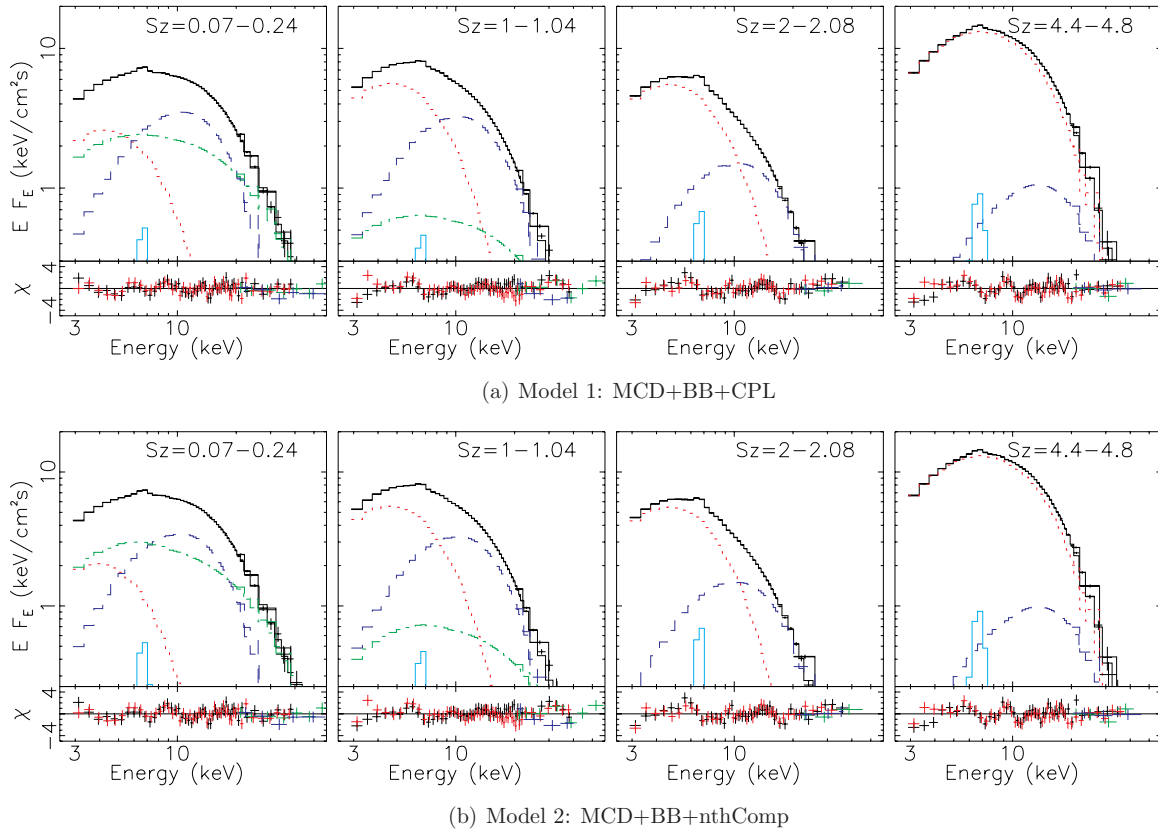
(a) Model 1: MCD+BB+CPL

(b) Model 2: MCD+BB+nthComp

Figure 5. Unfolded spectra and fit residuals for Models 1 and 2 at different positions in the Z track. For the unfolded spectra, only spectra of PCU 2 and HEXTE Cluster A are shown for clarity. The total model fit is shown as a black solid line, the (unscattered) MCD component as a red dotted line, the BB component as a blue dashed line, the Comptonized component (CPL/nthComp) as a green dot-dashed line, and the Fe line as a cyan triple-dot-dashed line. For the fit residuals, the black, red, green, and blue data points are for the PCU 2, PCU 0, and HEXTE Clusters A and B, respectively.

(A color version of this figure is available in the online journal.)

the SIMPL model with the MCD as the input seed spectrum to our spectra at the top of the HB where the Comptonization is the strongest, we found some systematic fit residuals above 20 keV, with the data falling below the model prediction at high energies (similar to case A in Figure 4 using a PL to describe the Comptonization). A possible explanation for this is that there is a high-energy cutoff in the Comptonization emission (i.e., the corona temperature is close to or within the energy range of our data), which was not included in the SIMPL model for simplicity (Steiner et al. 2009b). To account for this, one option is to modify the SIMPL model to include a high-energy cutoff for the Comptonized component by multiplying it by, e.g., the *highecut* model in XSPEC. An alternative option is to replace SIMPL with a Comptonization model with the corona temperature as a parameter, such as the nthComp model (in XSPEC; Życki et al. 1999; Zdziarski et al. 1996; Lightman & Zdziarski 1987). The nthComp model approximates the Comptonization by solving the Kompaneets equation with a relativistic correction to energy transfer between photons and electrons. The input seed photons can be a BB or an MCD in spectral shape, and we assumed the latter throughout the paper. The key parameters of this model include the asymptotic PL photon index $\Gamma_{\mathrm{nthComp}}$, the corona electron temperature $kT_{\mathrm{e,nthComp}}$, the seed photon temperature, and the normalization N_{nthComp}.

In this paper, we present the results with the Comptonized component modeled with nthComp. We note that similar conclusions can also be drawn using the SIMPL model modified to include the high-energy cutoff. Then our second

model (Model 2 or model MCD+BB+nthComp, hereafter) is *wabs*(*diskbb* + *bbodyrad* + *nthcomp* + *gaussian*)*edge*, with the seed photon temperature tied to the temperature of the MCD component kT_{MCD}. With Model 2, our aim is to take into account the photons Compton scattered so as to track the behavior of the thermal disk emission prior to Compton scattering (denoted as MCDPS hereafter), as done in SIMPL. Therefore, we calculated the photon flux of the MCDPS by adding the photon flux of nthComp (the scattered part of the MCDPS) to that of the MCD component (the unscattered part) and then obtained the corresponding energy flux and normalization of the MCDPS by increasing those of the MCD component proportionally to the photon flux (the MCDPS temperature kT_{MCDPS} is the same as kT_{MCD}).

To have a better constrained estimate of the parameters of the Comptonized component, we fitted the HB spectra simultaneously with their $\Gamma_{\mathrm{nthComp}}$ and $kT_{\mathrm{e,nthComp}}$ tied to be the same, as we did for Model 1. We found that comparably good fits can be obtained using a large range of $\Gamma_{\mathrm{nthComp}}$, i.e., 2.0–2.7, with $kT_{\mathrm{e,nthComp}}$ of 5.6–7.3 keV correspondingly. This uncertainty is coupled to the uncertainty in the fraction of the thermal disk emission scattered into the Comptonization emission, with a larger scattering fraction inferred using a larger value of $\Gamma_{\mathrm{nthComp}}$. However, the parameters (the temperature and the normalization) of the MCDPS and the BB are much less affected. Allowing a high value of $\Gamma_{\mathrm{nthComp}}$ might have the risk of large interference between the thermal (especially the disk) and the Comptonized components, as similarly observed in the fits
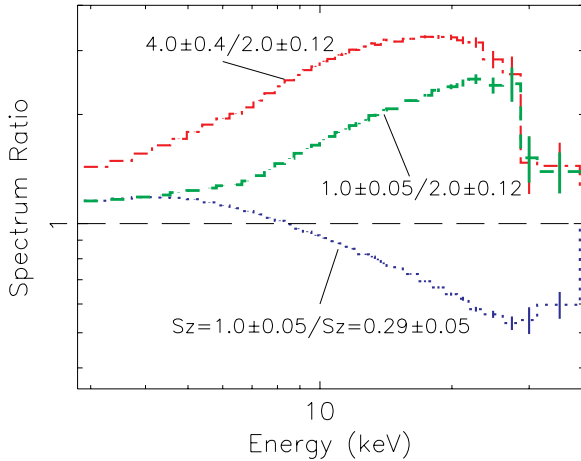
Figure 6. Ratios of the spectra on the two ends of each branch. Spectra with high total PCA intensity are divided by those with lower total PCA intensity in order to illustrate that on each branch the spectrum evolves differently.

(A color version of this figure is available in the online journal.)

to atoll-source X-ray spectra in Lin et al. (2007). In the end, we chose to present results using $\Gamma_{\rm nthComp} = 2.3$. Then the fit to all the HB spectra simultaneously gave $kT_{\rm e,nthComp} = 6.04 \pm 0.23$. The above values of $\Gamma_{\rm nthComp}$ and $kT_{\rm e,nthComp}$ were fixed in the final fits to all spectra. Sample fits with Model 2 are given in Figure 5(b). The systematic effect of our choice of $\Gamma_{\rm nthComp}$ will be discussed later by comparing with results using other values of $\Gamma_{\rm nthComp}$ in the range of 2.0–2.7.

We estimated $N_{\rm H}$ and $E_{\rm ga}$ with the two *Suzaku* observations. The energy bands and the data binning method used were the same as in Lin et al. (2010). We applied Model 1 (Model 2 gives very similar results) and fitted both *Suzaku* observations simultaneously with $N_{\rm H}$ and $E_{\rm ga}$ tied to be the same for both observations. Only a very weak CPL is needed in both observations. The absorption edge cannot be constrained by the data, probably because of the gap between the XIS and PIN (10–11 keV) and the relatively poor data quality around this edge. We still included it in the fit but fixed $E_{\rm edge} = 8.93$ keV (see above). Finally, we obtained $N_{\rm H} = (2.35 \pm 0.01) \times 10^{22}$ cm^{-2} and $E_{\rm ga} = 6.64 \pm 0.06$ keV. This $N_{\rm H}$ is consistent with $N_{\rm H} = (2.38 \pm 0.12) \times 10^{22}$ cm^{-2} obtained by Wroblewski et al. (2008) from the modeling of absorption edges found in *Chandra* high-resolution X-ray spectra.

4. RESULTS

4.1. Spectral Evolution

Figure 3 shows that the source goes back and forth between the HB and NB several times in the first 7 days and then up and down the FB many times in the last 2 days, but no clear secular changes are seen in Figure 2 (upper panels). As in LRH09, we calculate the ratios of spectra in different branches, which are shown in Figure 6. The blue dotted line is for the HB (the upper vertex divided by the top of the HB) and shows that the spectrum pivots around 9 keV, with the intensity below increasing and above decreasing as the source descends the HB. The green dashed line corresponds to the NB. Although the intensity increases over the whole energy range shown as the source evolves up the NB, the effect becomes stronger above ∼7 keV. The increase of the intensity on the FB is also mostly in the high energies 10–30 keV (red dot-dashed line). The ratios for the NB and FB drop sharply around 30 keV, above which

in fact there is no significant source emission. These ratios are similar to XTE J1701-462 in the Sco-like stage (LRH09).

The parameters derived from the spectral fits are shown in Figures 7–9 and are listed in Tables 1 and 2. For all luminosity (L) and radius (R) quantities, we assume a source distance of 12.6 kpc (Section 4.3), and the luminosities are based on bolometric fluxes of relevant spectral components (for the CPL component, we integrate over energies above 1 keV). Isotropic emission is assumed for all components (but see discussion in Section 5.2), except the MCD one, whose inclination i is assumed to be 60°. $R_{\rm BB}$ is the apparent radius of the BB component and is related to the normalization as $N_{\rm BB} \equiv (R_{\rm BB,km}/D_{10\,\rm kpc})^2$, where $D_{10\,\rm kpc}$ is the distance to the source in units of 10 kpc. $R_{\rm MCD}$ in Model 1 is the apparent inner disk radius and is calculated from the MCD normalization $N_{\rm MCD} \equiv (R_{\rm MCD,km}/D_{10\,\rm kpc})^2 \cos i$, while $R_{\rm MCDPS}$ in Model 2 is from the MCDPS normalization $N_{\rm MCDPS} \equiv (R_{\rm MCDPS,km}/D_{10\,\rm kpc})^2 \cos i$.

Figure 7 shows the luminosities of the thermal components MCD/MCDPS and BB versus their characteristic temperatures, while Figures 8 and 9 show the spectral fit results as a function of the rank number $S_{\rm Z}$. We included several constant radius lines in Figure 7, assuming $L_{\rm X} = 4\pi\sigma_{\rm SB} R^2 T^4$. The dotted and dot-dashed lines have $R = 8$ km ($N_{\rm BB} = 40$) and $R = 6.3$ km ($N_{\rm BB} = 25$), corresponding to the apparent sizes of the NS from the sum of the boundary layer and the burst emission and from only the burst emission, respectively (Section 4.3). The dashed lines have $R = 3$ km, shown for reference. The red solid lines describe the relation between $L_{\rm MCD}$ and $kT_{\rm MCD}$ with varying $R_{\rm MCD}$ at a constant $\dot{M}$, i.e., $L_{\rm MCD} \propto T_{\rm MCD}^{4/3}$ (LRH09; referring to the MCDPS in Model 2).

We focus on the results of Model 1 for the HB first. Figures 7 and 8 (left panels) show that $L_{\rm MCD}$ decreases and $L_{\rm CPL}$ increases as the source climbs up the HB, while $L_{\rm BB}$ changes much less. The anti-correlation between $L_{\rm MCD}$ and $L_{\rm CPL}$ is clear, as their sum (filled blue squares in the left panel (d) of Figure 8) changes by $\lesssim 10\%$ on the HB, much less than either individual component.

Model 2 assumes that some corona surrounds the thermal disk and produces the Comptonization emission. From this model, we also see the strong anti-correlation between the (unscattered) MCD component and the Comptonization emission (Figure 8). However, unlike Model 1, we see that the apparent inner disk radius from Model 2 (inferred from the MCDPS) increases as the source climbs up the HB. Moreover, the thermal disk based on the MCDPS follows a constant $\dot{M}$ line (the red solid line in Figure 7).

The Comptonized component becomes weak on the NB and is almost negligible on the FB (Figures 5 and 8), and the results of other components become very similar between Models 1 and 2 in these two branches. In Figures 7 and 8, both models show that in the NB the largest changes occur in the BB component. Its normalization varies by a factor of about 2.5, with the temperature hovering around 2.6 keV (Tables 1 and 2). This suggests that the change of intensity above ∼7 keV (green line in Figure 6) is mostly due to the BB component. However, since the BB is just a small component (<30% in terms of luminosity), the total luminosity only changes by ∼20% on the NB (Figure 8 and Tables 1 and 2).

The variations of the MCD/MCDPS component on the FB approximately follow a constant $\dot{M}$ line (the red solid line in Figure 7) from both models. The disk temperature increases from ∼1.7 keV at the lower vertex to nearly 3 keV at the top of the FB. Compared with the dotted line for the size of NS, the disk
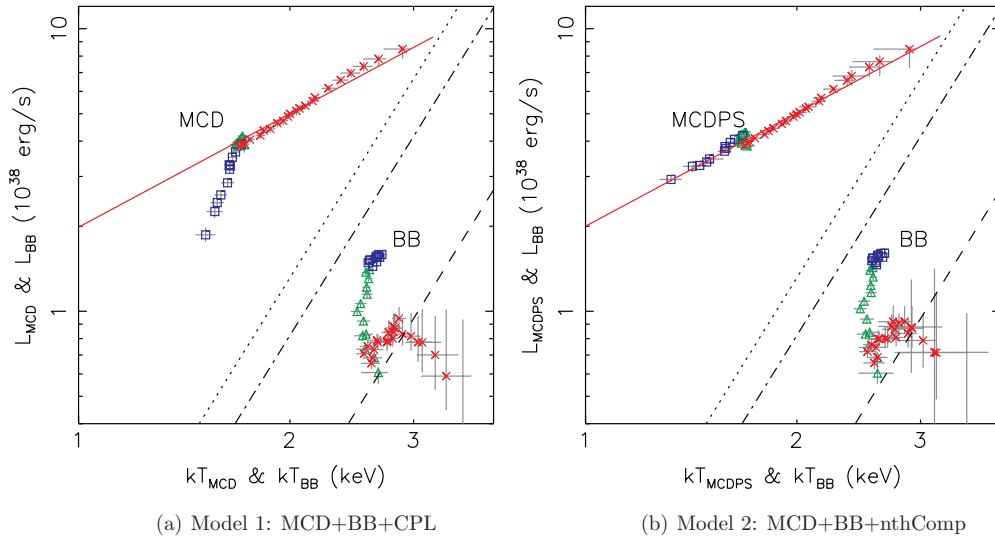
(a) Model 1: MCD+BB+CPL　　　　　　　　　　　　　　(b) Model 2: MCD+BB+nthComp

Figure 7. Fit results of S_Z-resolved spectra. The luminosities of the thermal components are plotted against their characteristic temperatures. The dotted, dot-dashed, and dashed lines correspond to $R = 8.0$, 6.3, and 3.0 km, respectively, assuming $L_X = 4\pi R^2 \sigma_{SB} T^4$, and the red solid line is a constant $\dot{M}$ line (see the text). Note that for Model 1 we plot the thermal disk emission unscattered and observed directly, while for Model 2 we plot the thermal disk prior to scattering.
(A color version of this figure is available in the online journal.)

is consistent with being truncated outside the NS. The results of the BB component show large uncertainties, especially in the upper part of the FB, making it difficult to infer the evolution trend of this component in this branch. This was also seen in the spectral fits of XTE J1701-462 in LRH09.

We have seen that the MCDPS from Model 2 evolves approximately along a constant $\dot{M}$ line over the whole Z track. The fractional rms of $\dot{M}$ using the relation of $\dot{M} \propto L_{MCDPS} R_{MCDPS}$ is about 6%. Assuming $L_{MCDPS} = kT_{MCDPS}^{\beta}$, we estimate the slope β by minimizing the χ^2 value defined as $\sum (y_i - \beta x_i - \alpha)^2 / (\epsilon_{yi}^2 + \beta^2 (\epsilon_{xi}^2 + \epsilon_0^2))$ (e.g., Tremaine et al. 2002), where $y = \log(L_{MCDPS})$ with 1σ error ϵ_y, $x = \log(T_{MCDPS})$ with 1σ error ϵ_x, $\alpha = \log(k)$, and the subscript i denotes the data points used. ϵ_0 is introduced to account for the possible systematic error r of kT_{MCDPS} ($\epsilon_0 = \log(1+r)$) and is set to such a value that the reduced χ^2 is one. We obtain $\beta = 1.36 \pm 0.07$ from data of the whole Z track, with $r = 2.4\%$ used. Consistent values of β can also be obtained using other choices of $\Gamma_{nthComp}$ in the range of 2.0–2.7 in Model 2.

Figure 9 shows the variations of the Fe K line and absorption edge using Model 1, while Model 2 gives very similar results. The line luminosity L_{line} first slightly decreases from the top of the HB to the upper vertex and then increases again until the end of the FB. It is highest on the FB. The line width σ_{line} is ~0.4 keV. The equivalent width EW_{line} peaks near the lower vertex, with a value of ~120 eV, and is ~60 eV around the upper vertex. The absorption depth at the edge energy τ_{edge} is around 0.05 and peaks at the lower part of the FB. We note that as *RXTE* data have only a modest energy resolution (~1.2 keV FWHM at 6.5 keV) the results of the Fe K line and absorption edge should be regarded with caution.

4.2. Comparison with Fast Variability

Figure 10 shows the rms integrated from the PDS (0.1–10 Hz) versus the Comptonization fraction inferred from Model 2. The same type of plot, substituting results from Model 1, has a very similar appearance. Both models infer low-Comptonization fraction (<10%) in the NB and FB, with significantly higher

values for the HB. The rms variations appear to be roughly correlated with the Comptonization fraction, and only the HB has rms >5%. In terms of these properties, the NB and FB are similar to the soft/thermal state of black hole X-ray binaries and atoll sources (Lin et al. 2007), while the HB is closer to their transitional/steep PL state. We note that the rms shows an enhancement near the lower vertex, which is due to the NB oscillations. We also note that the FB in fact shows large variability in light curves. The low rms obtained above to some extent is because we only integrate the rms above 0.1 Hz. Using a lower integration limit could result in a larger rms, as the PDS in the FB is steep, with a PL slope around 2 (Homan et al. 2002). In the above, we just use the same frequency range as in Lin et al. (2007) and LRH09 for fair comparison with their results.

Table 3 lists the HBOs (fundamental) and upper kHz QPOs that we detected in our data set. The dependence of their frequencies on S_Z is plotted in Figure 11. There are also other QPOs such as HBO second harmonics and lower kHz QPOs, which are not explored here due to their smaller ranges spanned in the Z track (Homan et al. 2002). The HBOs span the whole HB and NB ranging from about 20 to 60 Hz, while the upper kHz QPOs span the whole HB and a small upper part of the NB ranging from about 620 to 1000 Hz, generally consistent with the results in Homan et al. (2002). However, they found some upper kHz QPOs from around 1000 up to 1090 Hz on the middle NB, which we could hardly detect from our data. This is probably because they used more observations in their data analysis plus the fact that these QPOs are weak to begin with (rms <2%). The HBOs become broader on the lower NB, and their FWHM values have large uncertainties. Thus, we fixed the FWHM to be 15 Hz (Homan et al. 2002) in some fits.

Figure 12 shows the frequency of the upper kHz QPO versus R_{MCDPS} from Model 2. Assuming a relation of frequency = $k R_{MCDPS}^{\beta}$ and using the slope estimate method in Section 4.1, we obtain $\beta = -1.72^{+0.32}_{-0.49}$ (the dotted line in Figure 12; a systematic error of 2.3% is added for R_{MCDPS}) using only data on the HB and $\beta = -2.01^{+0.35}_{-0.51}$ (the dashed line; a systematic error of 2.1% is added for R_{MCDPS}) if data on the NB are also used. These values are consistent with -1.5 (the solid line, forced
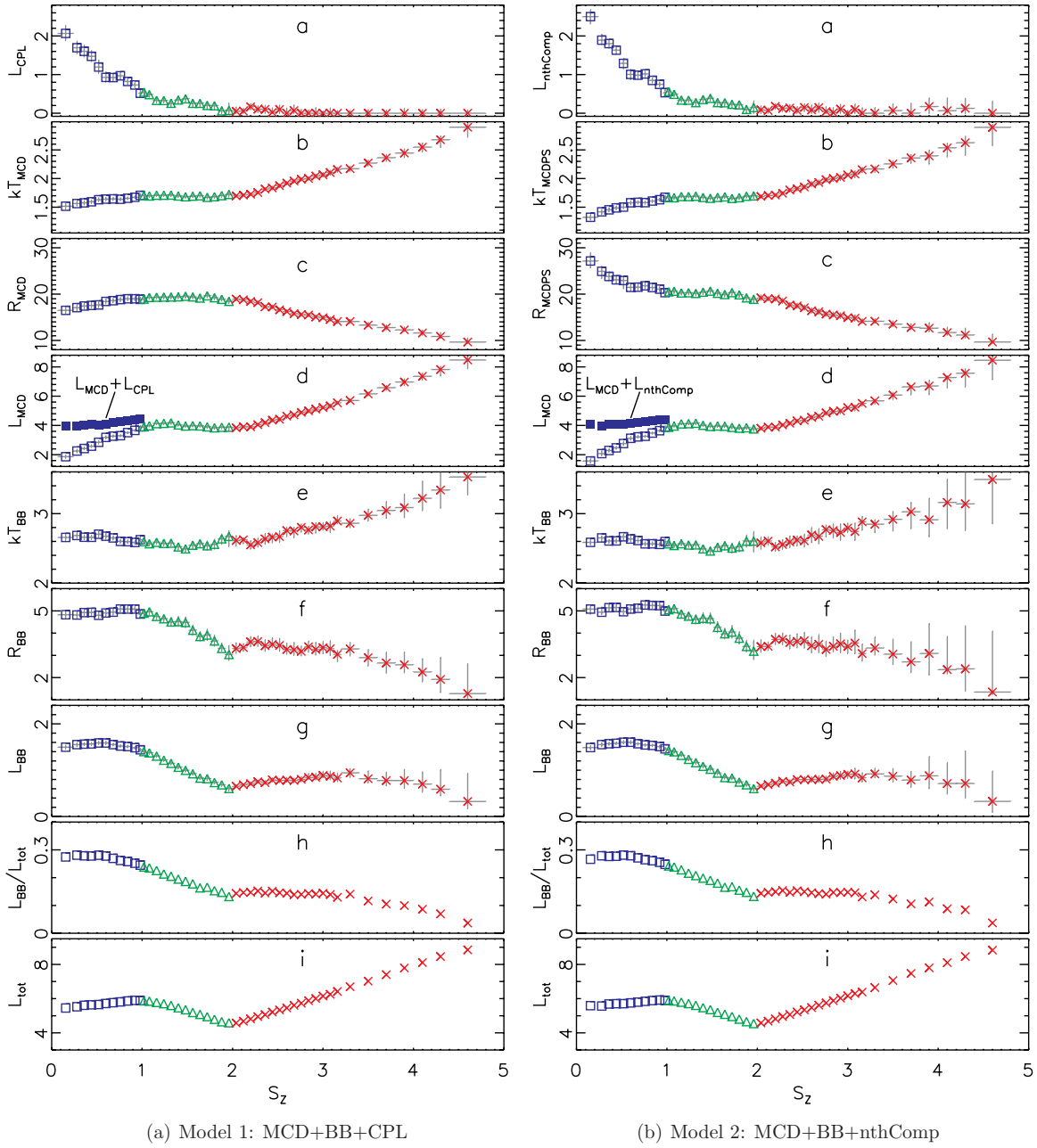
(a) Model 1: MCD+BB+CPL

(b) Model 2: MCD+BB+nthComp

Figure 8. Fit results of S_Z-resolved spectra as a function of the rank number S_Z. The error bar of S_Z corresponds to the range of S_Z for each spectrum. L_{tot} is the total luminosity, whose error bar is not plotted but is given in Tables 1 and 2. See the text for the meanings of other quantities. The units of the R, kT, and L quantities are km, eV, and 10^{38} erg s^{-1}, respectively.

(A color version of this figure is available in the online journal.)

to pass the data point with $S_Z = 0.96$–1.00), expected if the frequency of the upper kHz QPO is the Keplerian frequency at R_{MCDPS}. The systematic error of β due to our choice of $\Gamma_{nthComp}$ in Model 2 is estimated to be around 0.6 based on comparison with results using other values of $\Gamma_{nthComp}$ in the range of 2.0–2.7. In Model 1, R_{MCD} on the HB increases with the frequency of the upper kHz QPO. Therefore, it is important to note that the relationship between the upper kHz QPO frequency and the inner disk radius changes sign between the use of Models 1 and 2. The result shown in Figure 12 depends on a model that counts the number of Comptonized photons, so that the QPO frequency becomes correlated to the apparent inner radius of the disk prior to the effects of Compton scattering.

Figure 13 shows the frequency of the HBO versus R_{MCDPS} from Model 2. We see that the frequency of the HBO increases as R_{MCDPS} decreases down the HB, but both become relatively constant on the NB. We note that, in fact, the frequency of the HBO decreases slightly on the lower NB (Figure 11; Homan et al. 2002). Also assuming a relation of frequency $\propto R_{MCDPS}^{\beta}$, we estimate $\beta = -3.70^{+0.63}_{-0.96}$ (the dotted line in Figure 13; a systematic error of 1.6% added for R_{MCDPS}) using only data on the HB and $\beta = -4.35^{+0.66}_{-0.94}$ (the dashed line; a systematic error of 2.8% added for R_{MCDPS}) if data on the NB are also used. These values are roughly consistent with -3 (the solid line in Figure 13), a value expected in a Lense–Thirring interpretation of the HBO (Stella & Vietri 1998; van der Klis 2006). Based

Table 3
HBO Fundamental and Upper kHz QPOs

S_Z	HBO Fundamental			Lower kHz QPO			Upper kHz QPO		
	Frequency (Hz)	FWHM (Hz)	rms	Frequency (Hz)	FWHM (Hz)	rms	Frequency (Hz)	FWHM (Hz)	rms
0.07–0.24	22.0 ± 0.3	4.3 ± 1.3	0.032 ± 0.005				622.8 ± 28.3	$232.3^{+67.7}_{-97.0}$	0.064 ± 0.012
0.24–0.32	24.2 ± 0.5	$4.8^{+2.7}_{-1.6}$	0.029 ± 0.006				626.0 ± 21.1	$149.5^{+101.0}_{-58.1}$	0.055 ± 0.010
0.32–0.40	26.9 ± 0.3	5.7 ± 1.2	0.035 ± 0.004				$683.1^{+14.4}_{-20.6}$	$112.4^{+68.5}_{-38.1}$	0.042 ± 0.007
0.40–0.48	28.4 ± 0.3	$3.5^{+1.3}_{-0.9}$	0.024 ± 0.004				690.5 ± 17.3	156.9 ± 50.1	0.049 ± 0.007
0.48–0.56	29.8 ± 0.5	4.4 ± 1.6	0.028 ± 0.005				693.0 ± 32.4	$143.9^{+111.2}_{-63.2}$	0.042 ± 0.010
0.56–0.64	34.2 ± 0.7	$4.3^{+5.9}_{-2.3}$	$0.020^{+0.013}_{-0.005}$				741.9 ± 13.4	$79.3^{+64.9}_{-28.9}$	0.039 ± 0.008
0.64–0.72	36.6 ± 0.4	7.4 ± 1.6	0.030 ± 0.003				773.6 ± 23.8	205.5 ± 85.0	0.047 ± 0.008
0.72–0.80	39.6 ± 0.5	$8.7^{+2.3}_{-1.4}$	0.028 ± 0.003				797.0 ± 8.4	108.9 ± 25.0	0.040 ± 0.004
0.80–0.88	42.3 ± 0.5	9.4 ± 2.1	$0.027^{+0.003}_{-0.005}$	$518.2^{+8.1}_{-5.5}$	$22.1^{+21.5}_{-12.0}$	0.015 ± 0.004	827.3 ± 12.0	123.1 ± 35.0	0.036 ± 0.005
0.88–0.96	45.1 ± 0.7	9.2 ± 3.0	0.023 ± 0.004	552.6 ± 20.3	58.1 ± 36.0	0.017 ± 0.004	853.6 ± 12.9	110.9 ± 35.8	0.032 ± 0.005
0.96–1.00	$49.6^{+1.0}_{-2.9}$	$4.5^{+12.2}_{-3.2}$	$0.014^{+0.013}_{-0.006}$				899.3 ± 26.2	$141.4^{+104.4}_{-65.9}$	0.036 ± 0.010
1.00–1.04	52.3 ± 0.9	$4.5^{+4.3}_{-2.3}$	0.017 ± 0.005	619.5 ± 22.9	67.1 ± 35.9	0.026 ± 0.007	$891.3^{+59.7}_{-17.6}$	$34.6^{+188.2}_{-34.6}$	$0.018^{+0.016}_{-0.010}$
1.04–1.12	53.3 ± 1.7	$2.1^{+12.8}_{-1.9}$	$0.009^{+0.007}_{-0.004}$	653.6 ± 12.0	$48.3^{+38.8}_{-21.9}$	0.021 ± 0.005	962.7 ± 45.5	174.5 ± 110.5	0.028 ± 0.013
1.12–1.20	57.2 ± 0.9	5.9 ± 2.7	0.015 ± 0.003	690.3 ± 16.1	70.9 ± 28.6	0.024 ± 0.004	947.1 ± 16.0	$65.0^{+46.7}_{-31.6}$	0.021 ± 0.006
1.20–1.28	59.6 ± 0.7	3.3 ± 2.4	0.014 ± 0.003						
1.28–1.36	60.0 ± 0.7	4.0 ± 3.2	$0.018^{+0.004}_{-0.007}$						
1.36–1.44	60.9 ± 1.8	$0.9^{+19.5}_{-0.8}$	0.011 ± 0.004						
1.44–1.52	56.4 ± 5.7	15.0	0.017 ± 0.004						
1.52–1.60	53.3 ± 4.0	$16.4^{+11.7}_{-6.7}$	0.023 ± 0.005						
1.60–1.68	$55.3^{+4.9}_{-9.1}$	15.0	0.018 ± 0.005						
1.68–1.76	$54.5^{+2.7}_{-4.4}$	$13.7^{+16.7}_{-8.1}$	0.027 ± 0.008						
1.76–1.84	$53.8^{+10.5}_{-7.2}$	15.0	0.022 ± 0.006						
1.84–1.92	$51.0^{+4.6}_{-8.1}$	15.0	0.020 ± 0.006						
1.92–2.00	$44.5^{+5.0}_{-7.6}$	15.0	0.032 ± 0.007						

on the results using other choices of $\Gamma_{\rm nthComp}$, we estimate a systematic error of 1.2 for the above measurements of β.

4.3. The Source Luminosity Based on Type I X-Ray Bursts

Type I X-ray bursts in NS LMXBs can provide critical reference quantities such as the Eddington flux and the apparent NS surface area when they show photospheric radius expansion. These quantities can be compared with the spectral modeling results to infer the source luminosity and the visible size of the boundary layers, which are key elements in constructing the physical picture of the accretion process (Lin et al. 2007, 2010; LRH09). GX 17+2 shows both short (∼10 s) and long (≳100 s) bursts (Kuulkers et al. 2002; Galloway et al. 2008). With the persistent emission comparable to the peak net burst emission, these bursts are probably observed at accretion rates around the Eddington limit and are not expected (Galloway et al. 2008; Remillard et al. 2006). There is still debate as to how to analyze bursts at such high accretion rates. In the "standard" burst analysis, burst spectra are obtained by subtracting the persistent emission from the total emission and then fitted with a simple BB model. At high accretion rates, the persistent emission from the boundary layer may be strong. If it varies during bursts, it is instead probably more appropriate to fit the total emission with multiple spectral components, typically including a BB to describe the burst emission (e.g., Sztajno et al. 1986).

Kuulkers et al. (2002) applied the "standard" analysis to 10 bursts of GX 17+2 from *RXTE* data and obtained successful fits for most of them. Here, we combine our spectral modeling results of the persistent emission with their burst analysis to infer the Eddington flux and apparent NS area. In our data set, there are no short bursts but five long ones, corresponding to bursts 6–10 in Kuulkers et al. (2002). Burst 10 is near the lower vertex ($S_Z = 2.18$) but shows no photospheric radius expansion. Bursts 6–9 are near the upper vertex ($S_Z = 0.86$, 1.04, and 0.73, respectively) and show photospheric radius expansion, and we focus on them. In these bursts, for several tens of seconds right after the touch-down (the moment when the expanded matter falls back onto the NS surface), the burst temperatures peak and hover around ≃2.65 keV, and the apparent net burst area is roughly constant ($N_{\rm BB} \simeq 25$), corresponding to a peak net burst flux around 1.24×10^{-8} erg cm^{-2} s^{-1} (from burst 6). In comparison, the boundary layer during the persistent emission has a similar temperature and $N_{\rm BB} \simeq 15$ from our modeling, about a size of 60% of the net burst area.

With such a strong boundary layer, the Eddington flux and the apparent NS area would be very different depending on whether we infer them only from the net burst emission or have the boundary layer emission also included. We note this is not a serious issue in atoll sources, as their boundary layers are small (≲10% of the NS surface) and have temperatures typically lower than the bursts (Lin et al. 2007, 2010; LRH09). Considering that both the boundary layer and the burst emission are from the NS surface, we add them together and obtain the Eddington flux of about 2.0×10^{-8} erg cm^{-2} s^{-1} and the total apparent NS surface area of $N_{\rm BB} \simeq 40$ for GX 17+2, but we also discuss the results with the Eddington flux and the total NS apparent area calculated from the burst emission only.

The luminosities in Tables 1 and 2 are in units of the Eddington flux obtained above, and they would be 60% larger
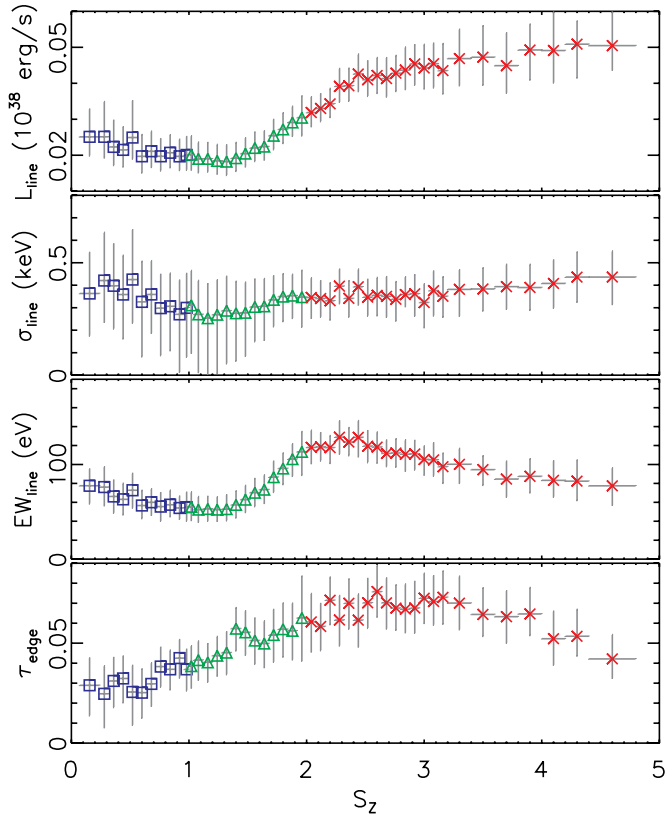
Figure 9. Fit results of Gaussian Fe line as a function of the rank number S_Z using Model 1.

(A color version of this figure is available in the online journal.)
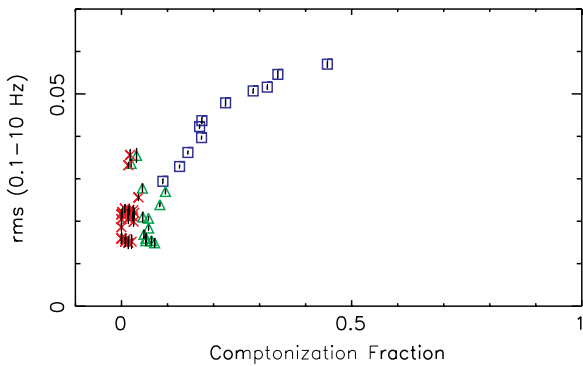

Figure 10. Fractional rms vs. the luminosity fraction of the Comptonized component, i.e., nthComp, obtained with Model 2.

(A color version of this figure is available in the online journal.)

Figure 11. Dependence of the frequencies of the upper kHz QPO and the HBO on S_Z.

(A color version of this figure is available in the online journal.)
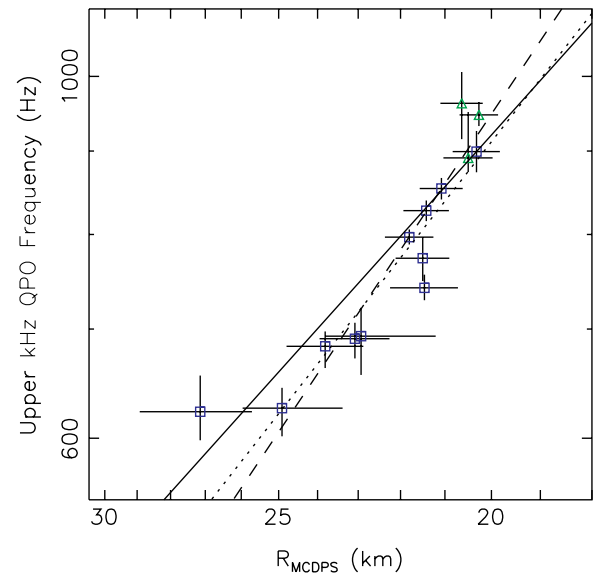
Figure 12. Frequency of the upper kHz QPO vs. the inner disk radius (prior to Compton scattering) from Model 2. The inner disk radius is derived from the MCDPS normalization, without corrections for factors such as the hardening effect. The solid, dotted, and dashed lines show the relation of frequency $\propto R_{MCDPS}^{\beta}$, with $\beta = -1.5$ (corresponding to the Keplerian frequency at the inner disk radius), -1.72 (from the fit to the HB data), and -2.01 (from the fit to the HB and NB data), respectively.

(A color version of this figure is available in the online journal.)

if we did not include the boundary layer emission in the calculation of the Eddington flux above. In the upper vertex, GX 17+2 has luminosity of a factor of 1.5 of the Eddington limit, higher than XTE J1701-462 in the Sco-like stage (below 0.9 Eddington luminosity; LRH09). If $\dot{M}$ accounts for different source types (Section 5.1), one might expect their luminosities to be similar. The above difference might be due to several uncertain factors, such as the inclination and the thickness of the accretion flow not taken into account in the Eddington flux correction above. However, we cannot rule out that their difference in luminosity is real, which could be due to factors such as different compositions of the accreted materials and different NS masses.

We estimate the source distance based on the Eddington flux obtained above. Using the empirical value of the Eddington luminosity of 3.79×10^{38} erg s^{-1} from Kuulkers et al. (2003), the source distance is 12.6 kpc, which is assumed in this paper. If the theoretical expression of the Eddington limit (see Equation (8) in Galloway et al. 2008) is used and an NS with a mass of 1.4 $M_{\odot}$ and a radius of 10 km is assumed, we obtain a source distance of 10.5 kpc for the H-poor case (the H-fraction $X = 0$) and 8.1 kpc for the H-rich case ($X = 0.7$). The above distances should increase by 26% if we only use the net burst emission to estimate the Eddington flux.
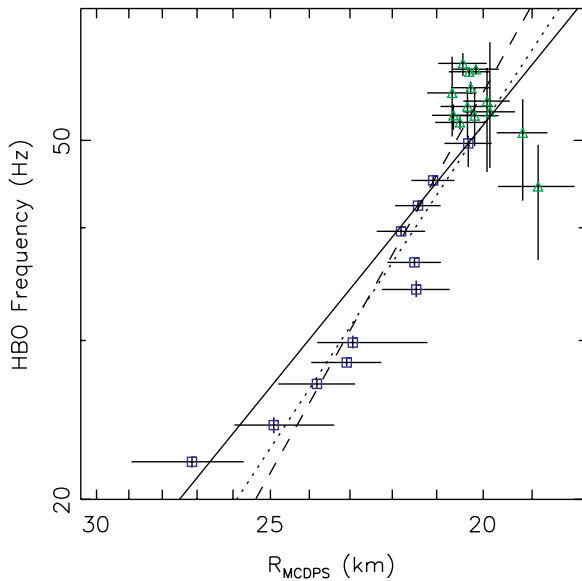
Figure 13. Frequency of the HBO vs. the apparent inner disk radius (prior to Compton scattering) from Model 2. The solid, dotted, and dashed lines show the relation of frequency $\propto R_{MCDPS}^{\beta}$, with $\beta = -3$ (corresponding to Lense–Thirring precession), -3.70 (from the fit to the HB data), and -4.35 (from the fit to the HB and NB data), respectively.

(A color version of this figure is available in the online journal.)

5. DISCUSSION

5.1. The Role of $\dot{M}$ in the Spectral Evolution

The spectral evolution of GX 17+2 along the Z track based on Model 1 (Figure 7(a)) is very similar to that of XTE J1701-462 in the Sco-like stage as obtained by LRH09 using a similar model. This supports the viability of physical interpretations for Z branch evolution offered in that paper (see Section 5.2). An associated question is whether the $\dot{M}$ into the disk varies along the Z track. LRH09 inferred a constant $\dot{M}$ along the Sco-like Z tracks of XTE J1701-462 based on the MCD component for the NB and FB. Although in the HB the MCD component did not follow a constant $\dot{M}$, the variation of the MCD luminosity was largely offset by that of the Comptonized component, leading LRH09 to surmise that on the HB $\dot{M}$ is also constant, with the thermal disk emission simply converted to the Comptonized emission as the source ascends the HB. Similar behavior observed in GX 17+2 using Model 1 implies that $\dot{M}$ is probably also constant in this system. Model 2 took a step further by providing an empirically self-consistent way to model the Comptonized component, assuming that a hot corona in the line of sight to the disk Comptonizes part of the thermal disk emission. We have seen an intriguing result of this model, i.e., L_{MCDPS}, the thermal disk luminosity prior to Compton scattering, is consistent with lying along a constant $\dot{M}$ line over the whole Z track (Figure 7). We note that in the above we use the MCDPS to infer the $\dot{M}$ into the disk. This assumes no significant mass loss around the area where most of the thermal disk emission is produced. At the very inner part of the disk, some of this $\dot{M}$ can be taken away by mass outflow (Section 5.2), with the rest going onto the NS surface to form the boundary layer. Based on the little variation of the total flux on the HB and NB seen in Di Salvo et al. (2000) and the comparison with black hole X-ray binaries, Homan et al. (2002) also suggested a constant $\dot{M}$ along the Z track.

The conclusion of a constant $\dot{M}$ into the disk along the Z track is further supported by the global evolution of GX 17+2. Its secular changes were observed to be very small, either from our data set spanning 9 days or from data spanning years in Wijnands et al. (1997) and Homan et al. (2002). This is in contrast with strong secular changes seen in XTE J1701-462 in 2006–2007, which were ascribed to the variation in the $\dot{M}$ into the disk (LRH09; Homan et al. 2007, 2010). Then a reasonable explanation for the lack of strong secular changes in GX 17+2 is that its $\dot{M}$ has been fairly constant. This interpretation implies a need of hardly varying $\dot{M}$ over its entire Z track, in accordance with our spectral fit results.

5.2. The Interpretation of Z Branches

If the $\dot{M}$ into the disk does not change along the Z track as argued above, the remaining main question is what causes the evolution along the Z track. Based on XTE J1701-462, LRH09 suggested that the three Sco-like branches are due to three physical processes operating at a constant $\dot{M}$ into the disk. The source climbs up the HB due to the increasing portion of the thermal disk emission Compton scattered. The excursion from the lower to the upper vertices on the NB corresponds to the transition from a standard-thin-disk accretion (Shakura & Sunyaev 1973) to a slim-disk accretion (Abramowicz et al. 1988). At the lower vertex, the disk is truncated at a radius outside the ISCO as the local Eddington limit is reached at the inner disk radius (see discussion below). The source climbs up the FB due to the temporarily fast decrease of the inner disk radius toward the ISCO. Since the source evolved slower and stayed longer in the two vertices than in other parts of Z tracks (at least on the NB and FB), the above three processes could correspond to three kinds of instability (LRH09). The slim-disk solution was associated with the upper vertex because it can provide more mass inflow onto the NS surface than the standard thin disk and can explain the increase of the BB apparent area from the lower to the upper vertices. The disk emission was not observed to change significantly during such a transition (in the Sco-like tracks), probably because the slim-disk emission differs from the standard disk significantly only at accretion rates much higher than the Eddington limit (Mineshige et al. 2000).

As a similar spectral evolution is observed in GX 17+2, the above picture can be applied to this system and is sketched in Figure 14. The disk is drawn to be thicker for the HB to represent a slim disk, and is thinner for the FB to represent a standard thin disk. On the HB, the disk is surrounded by a Comptonizing corona with a temperature of about 6 keV, based on our fits with Model 2 in this work. Nearly one half of the thermal disk is scattered at the top of the HB, but this quantity has a strong dependence on $\Gamma_{nthComp}$ (Section 3). The optical depth of the corona is about a few from Model 2, based on its relation with $\Gamma_{nthComp}$ and $kT_{e,nthComp}$ (Zdziarski et al. 1996). The Comptonized component is strong only at the top of the HB, making it hard to measure the variation of the optical depth along the Z track. Thus, we cannot easily infer whether the decrease of the Comptonization emission as the source descends the HB is due to the decrease of the covering fraction of the corona or due to the decrease of its optical depth.

We add some small arrows in Figure 14 to indicate the possible strong hot mass outflow at the very inner part of the accretion disk in this system. This is expected to be a common phenomenon for a disk accretion system at high accretion rates, in which the mass can be input into the disk from outside and
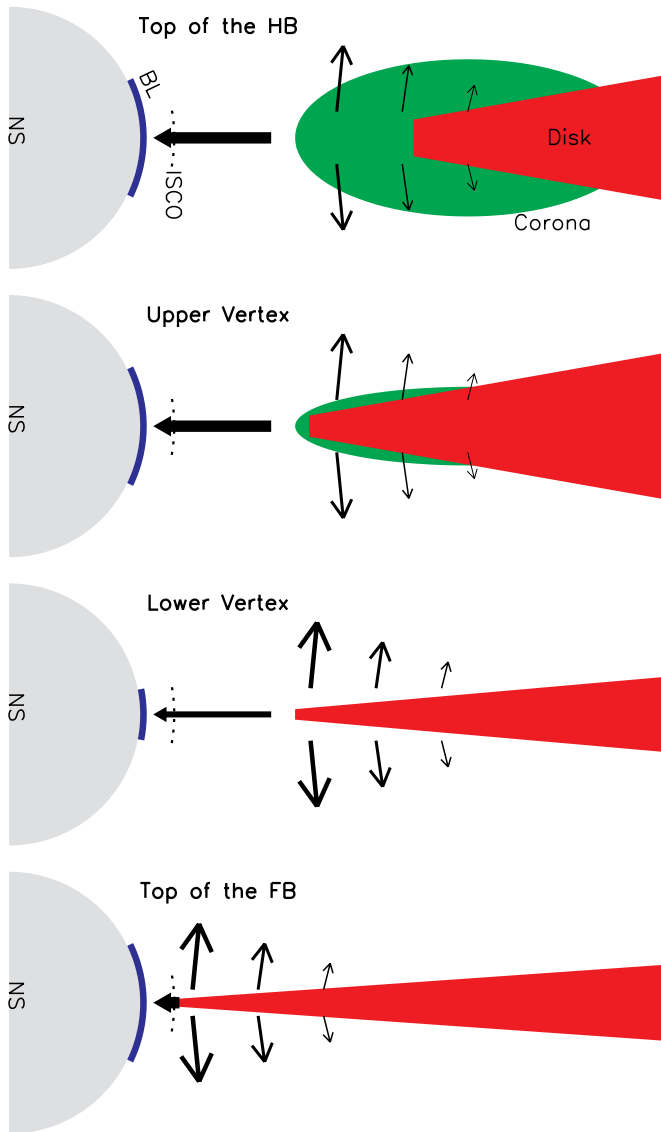
Figure 14. Schematic sketch of the accretion flow at different positions of the Z track. The system is assumed to be axisymmetric relative to the rotational axis, and the sketch shows one half of the cross-section through the rotational axis. Arrows represent the mass flow onto the NS surface and out of the disk (at the inner disk), with the strength roughly indicated by the thickness of the arrows. The blue arc represents the boundary layer (BL).

(A color version of this figure is available in the online journal.)

ejected as a disk wind at the very inner part of the disk where the emission perpendicular to the disk plan reaches the local Eddington limit (Katz 1980; Watarai et al. 2000; Mineshige et al. 2000; Fukue 2004; Ohsuga & Mineshige 2007). The mass outflow can also explain the low BB luminosity, relative to the disk luminosity (discussed below).

Figure 14 does not include the jet component that is possibly responsible for the radio emission detected from this system. Migliari et al. (2007) observed the radio emission to decrease significantly from the HB to the FB along the Z track and found it to correlate with a hard spectral component (the "hard tail"), which they fitted with a PL. In this paper, we used a different data set and a different spectral model from those used by Migliari et al. (2007). However, we found that consistent results can also be obtained if we fitted our data with their model (the same as the one used by Di Salvo et al. 2000).

The CPL/nthComp component in our model was also observed to decrease significantly from the HB to the FB, in a similar way as the hard tail in Migliari et al. (2007), thus probably also correlating with the radio emission. It played a similar role as the PL component in Migliari et al. (2007) in that both of them are the dominating spectral component at energies above 30 keV when they are the strongest, at the top of the HB. We have shown that the CPL/nthComp model described our data better than the PL model (Figure 4). We note that the HB spectra in Migliari et al. (2007) seemed to extend above 60 keV, which was not seen in our HB spectra. The 60–100 keV HEXTE count rates are about three σ and about 2% of the background level in their HB observation 70023-01-01-00. To check whether the apparent lack of the hard tail above 60 keV in our data is due to relatively small exposures of our S_Z-resolved spectra (each with a few ks at the top of the HB, compared with ~10 ks for the spectrum in Migliari et al. 2007), we combined the spectra of the first five S_Z selections (representing the upper half of the HB, where the hard tail was reported to be strongest), resulting in a spectrum with an exposure time of ~20 ks. We found that the source was detected at less than one σ in the 60–100 keV band (combining data from both HEXTE clusters), suggesting that this (additional) hard emission may be transient, even for the same location in the Z track.

The hard tail observed by *BeppoSAX* from GX 17+2 in the HB has been explained in two different models, i.e., hybrid Comptonization and bulk motion Comptonization, by Farinelli et al. (2005) and Farinelli et al. (2007), respectively. In the hybrid Comptonization model (using the *eqpair* model (Coppi 1999) in XSPEC), two electron populations (thermal and non-thermal) are required, with the non-thermal one accounting for most of the hard tail above ~30 keV. In the bulk motion Comptonization model (using the *bmc* model (Titarchuk et al. 1997) in XSPEC), the hard tail is caused by Compton upscattering of soft photons by energetic electrons in a converging flow onto the NS. The hard component (CPL/nthComp) in our HB spectra has an exponential cutoff at ~10 keV and has been explained by us as due to Comptonization by a low-temperature (~6 keV) thermal corona covering the accretion disk (i.e., the non-thermal electron population is not needed). The bulk motion Comptonization model cannot explain this component easily because the cutoff energy of its emergent spectrum is much higher (a few hundred keV; Titarchuk et al. 1997).

In Figure 14 the boundary layer, which we model with a BB, is pictured as an equatorial belt on the NS surface. On the HB, N_{BB} of the boundary layer is around 15, while the entire NS surface has a corresponding value of 40 if we sum the boundary layer area and the burst emission area together (Section 4.3), indicating that the boundary layer has an apparent fraction of 3/8 of the entire NS surface. The real fraction is different, because of the special geometry of the boundary layer pictured above, and can be estimated following Lin et al. (2007). We infer the maximal latitude of the boundary layer to be 26° and 35°, corresponding to 43% and 57% of the entire NS surface, for an inclination of 60° and 30°, respectively. In the lower vertex, the boundary layer has $N_{BB} \sim 6$, and we infer the maximal latitude of the boundary layer to be 11° and 18°, corresponding to 19% and 30% of the entire NS surface, for an inclination of 60° and 30°, respectively. The solutions for an inclination of 60° are used to create Figure 14, except for the panel for the top of the FB, which is arbitrary due to large uncertainty. The above estimates of the size of the boundary layer are only approximate, neglecting factors such as the thickness of accretion flow, and

should be larger if we estimate the NS surface area only from the burst emission area. The above corrections imply that the real boundary layer luminosities should be higher than those shown in Figures 7 and 8 by up to 50%. However, even with such corrections, the luminosity of the boundary layer seems to be still less than the disk luminosity, which is not expected from the simple energy argument (Mitsuda et al. 1984). One explanation for this is the mass outflow described above.

Although large uncertainties are seen on the FB (Section 4.1), the boundary layer on the HB and NB has temperatures around 2.6 keV, about the peak value seen in the radius expansion bursts from this system (Kuulkers et al. 2002). This indicates that the boundary layer emission may have reached the local Eddington limit. In such a situation, the increase in the mass accretion rate onto the NS surface will just lead to increase in the boundary layer emission area (not its temperature), as seen on the NB. This was also observed in XTE J1701-462 (LRH09).

5.3. The Origins of kHz QPOs and HBOs

We have found that the dependence of the frequency of the upper kHz QPO on the apparent inner disk radius R_{MCDPS} is roughly consistent with frequency $\propto R_{MCDPS}^{-3/2}$ from Model 2, making it natural to identify it as the Keplerian frequency at the inner disk radius. This has been a critical assumption in many explanations of the kHz QPOs (Lin et al. 2011; van der Klis 2006). We note that R_{MCDPS} has been corrected for the photons that we assumed to be from the thermal disk emission but scattered by the corona. We also caution that the absolute values of the radius measurements have scale uncertainties that depend on the source distance, the inclination, the hardening effect, and the NS mass (Zhang et al. 1997). There is another important factor (η in Zhang et al. 1997) to account for the difference between the real inner disk radius and the radius where the disk temperature peaks. All these factors have too large uncertainties to allow for a meaningful estimate of the real inner disk radius directly from R_{MCDPS}. We calculated the variation of the upper kHz QPO with R_{MCDPS} to infer its dependence on the real inner disk radius, assuming that the above conversion factors between R_{MCDPS} and the real inner disk radius are fairly constant, at least along the Z track where upper kHz QPOs are observed.

The frequency of the HBO is too low to be the Keplerian frequency at the inner disk radius. However, we also observe its close dependence on R_{MCDPS} covering the entire HB and NB. Thus, the HBO is probably intimately related to the dynamics at the inner disk radius in some way. In the Lense–Thirring interpretation for the HBO, an approximate relation of frequency $\propto R_{MCDPS}^{-3}$ is expected (Stella & Vietri 1998; van der Klis 2006), and our results are roughly consistent with this. Although frequency of the HBO varies much less on the NB than on the HB, it still shows a small increase first and then a small decreases as the source descends the NB (Figure 11; Homan et al. 2002). The error bars of R_{MCDPS} are not small enough for us to conclude whether or not it correlates with this evolution pattern. However, we cannot rule out that such an evolution of the HBO on the NB is due to the change of the disk structure from a slim disk to a standard thin disk on the NB (Section 5.3). The decrease in the quality of the HBO on the lower NB (Homan et al. 2002) might be related to this.

6. CONCLUSIONS

We have analyzed a Z track of GX 17+2 from *RXTE* observations between 1999 October 3 and 12. Our analysis has

confirmed similar spectral properties of GX 17+2 to those of XTE J1701-462 in the Sco-like stage. In this study, we took a further step by modeling the Comptonized component in an empirically self-consistent way and found that the evolution of the thermal disk is consistent with being at a constant $\dot{M}$ into it over the whole track, supporting our conclusion of a constant $\dot{M}$ over the whole Sco-like Z track. Similar to XTE J1701-462, we found that the branches of GX 17+2 can be explained as being due to three processes operating at a constant $\dot{M}$ into the disk. The HB is due to increase of the Comptonization with respect to the upper vertex. The FB is due to shrinking of the inner disk radius on fast timescales from the lower vertex. On the NB we saw variation in the area of the boundary layer, which can be explained as being due to transition from accretion through a slim disk in the upper vertex to a standard thin disk in the lower vertex. The boundary layer has a size of ∼20%–30% of the entire NS surface in the lower vertex and ∼40%–60% in the upper vertex and is probably at the local Eddington limit.

The dependence of the frequency of the upper kHz QPO on the apparent inner disk radius is found to be roughly consistent with frequency $\propto R_{MCDPS}^{-3/2}$ on the HB, supporting identification of the frequency of the upper kHz QPO as the Keplerian frequency at the inner disk radius. We measure frequency $\propto R_{MCDPS}^{-4.0\pm0.7}$ for the HBO over the entire HB and NB, indicating an intimate relation between the HBO and the dynamics at the inner disk.

REFERENCES

Abramowicz, M. A., Czerny, B., Lasota, J. P., & Szuszkiewicz, E. 1988, ApJ, 332, 646
Barret, D. 2001, Adv. Space Res., 28, 307
Barret, D., Bachetti, M., & Miller, M. C. 2011, ApJ, 728, 9
Coppi, P. S. 1999, in ASP Conf. Ser. 161, High Energy Processes in Accreting Black Holes, ed. J. Poutanen & R. Svensson (San Francisco, CA: ASP), 375
Di Salvo, T., Stella, L., Robba, N. R., et al. 2000, ApJ, 544, L119
Farinelli, R., Frontera, F., Zdziarski, A. A., et al. 2005, A&A, 434, 25
Farinelli, R., Titarchuk, L., & Frontera, F. 2007, ApJ, 662, 1167
Fukue, J. 2004, PASJ, 56, 569
Galloway, D. K., Muno, M. P., Hartman, J. M., Psaltis, D., & Chakrabarty, D. 2008, ApJS, 179, 360
Hasinger, G., & van der Klis, M. 1989, A&A, 225, 79
Hasinger, G., van der Klis, M., Ebisawa, K., Dotani, T., & Mitsuda, K. 1990, A&A, 235, 131
Hertz, P., Vaughan, B., Wood, K. S., et al. 1992, ApJ, 396, 201
Homan, J., van der Klis, M., Fridriksson, J. K., et al. 2010, ApJ, 719, 201
Homan, J., van der Klis, M., Jonker, P. G., et al. 2002, ApJ, 568, 878
Homan, J., van der Klis, M., Wijnands, R., et al. 2007, ApJ, 656, 420
Hurkett, C. P., Vaughan, S., Osborne, J. P., et al. 2008, ApJ, 679, 587
Jahoda, K., Swank, J. H., Giles, A. B., et al. 1996, Proc. SPIE, 2808, 59
Katz, J. I. 1980, ApJ, 236, L127
Koyama, K., Tsunemi, H., Dotani, T., et al. 2007, PASJ, 59, 23
Kuulkers, E., den Hartog, P. R., in't Zand, J. J. M., et al. 2003, A&A, 399, 663
Kuulkers, E., Homan, J., van der Klis, M., Lewin, W. H. G., & Méndez, M. 2002, A&A, 382, 947
Kuulkers, E., van der Klis, M., Oosterbroek, T., et al. 1994, A&A, 289, 795
Kuulkers, E., van der Klis, M., Oosterbroek, T., van Paradijs, J., & Lewin, W. H. G. 1997, MNRAS, 287, 495
Levine, A. M., Bradt, H., Cui, W., et al. 1996, ApJ, 469, L33
Lightman, A. P., & Zdziarski, A. A. 1987, ApJ, 319, 643
Lin, D., Remillard, R. A., & Homan, J. 2007, ApJ, 667, 1073
Lin, D., Remillard, R. A., & Homan, J. 2009, ApJ, 696, 1257
Lin, D., Remillard, R. A., & Homan, J. 2010, ApJ, 719, 1350
Lin, Y.-F., Boutelier, M., Barret, D., & Zhang, S.-N. 2011, ApJ, 726, 74
Migliari, S., Miller-Jones, J. C. A., Fender, R. P., et al. 2007, ApJ, 671, 706
Mineshige, S., Kawaguchi, T., Takeuchi, M., & Hayashida, K. 2000, PASJ, 52, 499
Mitsuda, K., Inoue, H., Koyama, K., et al. 1984, PASJ, 36, 741
Ohsuga, K., & Mineshige, S. 2007, ApJ, 670, 1283
Protassov, R., van Dyk, D. A., Connors, A., Kashyap, V. L., & Siemiginowska, A. 2002, ApJ, 571, 545
Remillard, R. A., Lin, D., Cooper, R. L., & Narayan, R. 2006, ApJ, 646, 407

Rothschild, R. E., Blanco, P. R., Gruber, D. E., et al. 1998, ApJ, 496, 538
Sanna, A., Méndez, M., Altamirano, D., et al. 2010, MNRAS, 408, 622
Shakura, N. I., & Sunyaev, R. A. 1973, A&A, 24, 337
Steiner, J. F., McClintock, J. E., Remillard, R. A., Narayan, R., & Gou, L.
    2009a, ApJ, 701, L83
Steiner, J. F., Narayan, R., McClintock, J. E., & Ebisawa, K. 2009b, PASP,
    121, 1279
Stella, L., & Vietri, M. 1998, ApJ, 492, L59
Sztajno, M., van Paradijs, J., Lewin, W. H. G., et al. 1986, MNRAS, 222, 499
Takahashi, T., Abe, K., Endo, M., et al. 2007, PASJ, 59, 35

Titarchuk, L., Mastichiadis, A., & Kylafis, N. D. 1997, ApJ, 487, 834
Tremaine, S., Gebhardt, K., Bender, R., et al. 2002, ApJ, 574, 740
van der Klis, M. 2006, in Compact Stellar X-ray Sources, ed. W. Lewin & M.
    van der Klis (Cambridge: Cambridge Univ. Press), 39
Watarai, K.-y., Fukue, J., Takeuchi, M., & Mineshige, S. 2000, PASJ, 52, 133
Wijnands, R., Homan, J., van der Klis, M., et al. 1997, ApJ, 490, L157
Wroblewski, P., Guver, T., & Ozel, F. 2008, arXiv:0810.0007
Zdziarski, A. A., Johnson, W. N., & Magdziarz, P. 1996, MNRAS, 283, 193
Zhang, S. N., Cui, W., & Chen, W. 1997, ApJ, 482, L155
Życki, P. T., Done, C., & Smith, D. A. 1999, MNRAS, 309, 561